Computers and Fluids 223 (2021) 104952

Contents lists available at ScienceDirect

Computers and Fluids

journal homepage: www.elsevier.com/locate/compfluid

Intrusive generalized polynomial chaos with asynchronous time integration for the solution of the unsteady Navier–Stokes equations

P. Bonnaire [a], P. Pettersson [b,*], C.F. Silva [a]

[a] Group of Thermo-Fluid Dynamics, Technical University of Munich, Germany
[b] NORCE Norwegian Research Centre, Norway

ARTICLE INFO

Article history:
Received 16 April 2020
Revised 5 March 2021
Accepted 29 March 2021
Available online 2 April 2021

Keywords:
Generalized polynomial chaos
Stochastic Galerkin projection
Navier–Stokes equations
Kármán vortex street

ABSTRACT

Generalized polynomial chaos provides a reliable framework for many problems of uncertainty quantification in computational fluid dynamics. However, it fails for long-time integration of unsteady problems with stochastic frequency. In this work, the asynchronous time integration technique, introduced in previous works to remedy this issue for systems of ODEs, is applied to the Kármán vortex street problem. For this purpose, we make use of a stochastic clock speed that provides the phase shift between the realizations and enables the simulation of an in-phase behavior. Results of the proposed method are validated against Monte Carlo simulations and show good results for statistic fields and point-wise values such as phase portraits, as well as PDFs of the limit cycle. We demonstrate that low-order expansions are sufficient to meet the demands for some statistic measures. Therefore, computational costs are still competitive with those of the standard form of intrusive generalized polynomial chaos (igPC) and its non-intrusive counterpart (NigPC).

1. Introduction

Generalized polynomial chaos (gPC) [1–4] is an uncertainty quantification (UQ) approach devoted to the propagation of uncertainties from inputs to outputs of a numerical model, e.g., discretized partial differential equations. In this method, a series expansion in orthogonal basis functions or modes is applied to the model, i.e., each stochastic variable is described as a linear combination of stochastic modes. The modes are generally orthogonal polynomial functions of standardized random variables with known statistical properties. The Quantities of Interest (QoIs), which are directly related to the output(s) of the model, are also described by a linear combination of well-known stochastic modes. As a result, the UQ problem reduces to the finding of the gPC coefficients describing the QoIs. There are two classes of methods for their evaluation: Non-intrusive generalized polynomial chaos (NigPC) and intrusive generalized polynomial chaos (igPC).

NigPC has consolidated in the past years as an approach to perform UQ on systems characterized by complex numerical models that describe steady QoIs [5–9]. Non-intrusive methods rely on random or deterministic sampling. The former case includes random discrete L^2 projection [10], sparse gPC based on least angle regression [11], and compressive sampling for identification of sparse gPC approximations [12]. In the case of deterministic sampling instead, the QoI is evaluated at carefully chosen points in parameter space, e.g., Gauss points. Once the input random variables are discretized – following one of the two aforementioned methods – a collection of representative samples is generated in the stochastic space. Subsequently, associated deterministic numerical simulations are performed, where each simulation can be understood as a realization, i.e., a sample of a stochastic simulation. Provided that the QoI is a sufficiently smooth function of the uncertain input parameters, the number of deterministic simulations needed is considerably smaller than in other sampling based methods, such as Monte-Carlo simulation or Latin-Hypercube methods. For very large numbers of random variables, the smoothness requirements and computational cost become prohibitive (the curse of dimensionality). This can to some extent be remedied by model reduction to limit the number of input random variables and the number of basis functions, in particular for elliptic problems [13]. Further methods used to improve the rate of convergence with respect to the number of total terms in the series expansion for linear, elliptic Partial Differential Equations (PDEs) with different functional uncertainties in the diffusion coefficient are presented in Bachmayr et al. [14,15], which are based on the results from [16]. Anisotropic Smolyak type polynomial spaces can alleviate the curse of dimensionality under proper smoothness assumptions of the parameter random fields [17,18].

* Corresponding author.
E-mail address: pepe@norceresearch.no (P. Pettersson).

https://doi.org/10.1016/j.compfluid.2021.104952
0045-7930/

NigPC has been applied in a plethora of applications, where the QoIs are generally scalar, steady quantities. For example, investigations where: uncertainties in the Young's moduli of a structure model induce uncertainties in the deflection of a truss structure [19]; uncertainties in geometrical parameters of a truncated cone induce uncertainties in the flow, described by the Euler Equations, and in the corresponding (steady) pressure, which is measured at some specific locations [7]; uncertainties in the thermal conductivity of the heat equation induce uncertainties in the (steady state) temperature [20]; uncertainties in the Smagorinsky model of a Large Eddy Simulation induce uncertainties in the statistical moments of decaying homogeneous isotropic turbulence [5]; uncertainties in the Smagorinsky coefficient characterized by a reactive Large Eddy Simulation induce uncertainties in the mean and rms values of velocity, temperature and mixture fraction at specific locations [9]. In contrast, few works have been carried out, where the QoIs are steady *field* quantities. For example, Onorato et al. [21], while using the 2D Turbulent Navier–Stokes equations, investigated how uncertainties in the angle of attack of an airfoil induced uncertainties in the field of Mach number. Congedo et al. [6] investigated how uncertain inflow conditions induced uncertainties in the field of mean velocity of a turbulent swirled flow modeled by means of both Reynolds averaged Navier Stokes and Large Eddy Simulation. Note that in those cases the computational costs of NigPC are high, as the gPC coefficients associated to each point in the field of interest must be computed.

The intrusive counterpart of gPC rose considerable interest in the first decade of 2000's [22–27]. Contrary to NigPC, igPC by means of stochastic Galerkin projection is not a sampling based method: only one numerical simulation of an expanded model is needed to calculate the gPC coefficients, whether these are scalars or field quantities. The practical use of igPC may be limited due to the fact that standard numerical solvers, often the result of years of investigation, cannot be used without prior modification. Computational aspects of igPC formulations of the incompressible Navier–Stokes equations in the laminar flow regime were treated in Knio and Le Maître [28], and boundary conditions for a well-posed formulation and a stable numerical scheme were presented in Pettersson et al. [29].

A well-known limitation of gPC is its inaccuracy in uncertainty propagation of unsteady problems, where the phase between realizations changes over time, e.g., turbulent flows or flows exhibiting periodic behavior. In theory, unsteady stochastic problems can be accurately described by considering an infinite number of stochastic modes [30–32]. In practice, accounting for an infinite number of stochastic modes is infeasible. The energy in periodic systems, in contrast to turbulent flows, is usually distributed in a handful of frequencies. As a result, the phase shift between realizations of the stochastic periodic problem can be tracked. Two situations arise. (i) Deterministic frequencies: cases where the phase shift between realization is negligible, so that regular gPC is reliable and can be used without modification to study periodic flows. This fact is sometimes lost in claims in the scientific literature: "gPC ... cannot deal with the Navier–Stokes equations for unsteady noisy flows, such as flow past a stationary cylinder. For these problems gPC fails to converge after a short time" [33]; "gPC tends to break down for long-time integration" [34]; "A well-known difficulty is the simulation of uncertain time-dependent problems over long times" [35]; "note also that polynomial chaos could introduce convergence issues when dealing with unsteady flow problems" [6]. We would like to stress that the previous sentences may be misleading if the entire context of the associated studies is not carefully read. There are numerous problems regarding periodic oscillations, where regular gPC could be used to study uncertainty propagation. However, only few studies, such as Lucor and Karniadakis [24], have focused on this matter. (ii) Stochastic frequencies: cases where the phase shift between realizations is not negligible. Here standard igPC and NigPC fail to produce accurate results if the stochastic basis remains small [33]. Wan and Karniadakis [33] proposed multi-element gPC, where the stochastic space is partitioned into stochastic elements and standard gPC is independently applied to each element. Despite its accuracy, it is computationally much more expensive than regular gPC. Le Maître et al. [35] introduced asynchronous time integration (ATI) for igPC with rescaled time in the stochastic domain. The local time of each realization is adjusted so that all realizations remain in phase. If the phase shift between the realizations is smooth as a function of the input random variables, it is possible to derive an ordinary differential equation (ODE) that describes the adjustment of the clock. Schick et al. [36] proposed a method for the adjustment of the local time in cases where the phase shift between realizations is irregular. Schick et al. [36] argue that the ATI method is not robust enough for that purpose, and that it is preferable to use a robust optimization method to determine the clock adjustment, despite increased computational cost. Mai and Sudret [37] proposed time warping for phase adjustment for NigPC. Giraldi et al. [38] also used NigPC and a time shift to synchronize wave arrival times within an earthquake model. Conceptually related is the technique of introducing a physical coordinate transformation to align discontinuities in parameter space, applied to multi-layered sedimentary basins [39]. A different approach was proposed by Gerritsma et al. [34], where time-dependent gPC was introduced with new stochastic variables and orthogonal polynomials being constructed as time progresses. Consequently, the number of stochastic modes remains small as the associated basis is nearly optimal for a sufficiently small time interval.

Due to the constraints mentioned above, standard NigPC and igPC should be avoided for problems where the QoIs are periodic with stochastic frequencies, or turbulent. Accurate uncertainty propagation for turbulent or periodic (stochastic frequency) QoIs would bring significant advantages in many engineering applications. We want to stress, however, that a considerable amount of work (mostly in turbulent QoIs) still remains to attain that goal.

In this work, we investigate the Kármán vortex street generated by a flow around a rectangular cylinder by means of the incompressible Navier–Stokes equations. The following are the main objectives of the present study:

- To show that standard gPC is suitable for unsteady problems, where the QoIs are periodic and the frequency remains deterministic.
- To show that standard gPC fails when investigating periodic QoIs that exhibit stochastic frequencies. We want to warn that standard igPC and NigPC cannot be used to study such cases, or more complex cases regarding turbulent QoIs.
- To show that ATI-igPC works predominantly well in periodic flows that exhibit stochastic frequencies. This extends the work of Le Maître et al. [35], who introduced ATI-igPC for ordinary differential equations.
- To show advantages of igPC with respect to NigPC in terms of computational costs, when the QoIs of interest are *unsteady fields*.

The paper is structured as follows: In Section 2 the gPC series expansion is put in a wider context, and it is shown how ATI-igPC can be derived from a general series expansion. Section 3 explains the fundamentals of the ATI method. In Section 4, the gPC expanded set of equations for the incompressible Navier–Stokes equations is derived using the ATI method. Section 5 gives a brief overview of the statistical measures used in this work. The numerical results, including some information on the computational costs of the solver, are presented in Section 6 and conclusions are drawn in Section 7.

2. Series expansions of random fields

Consider a suitable probability space describing all relevant input uncertainties of the nonlinear space-time dependent model of interest. The elementary events of the space are denoted $\omega \in \Omega$, where Ω is the sample space. To represent and propagate uncertainty through the model, consider the general series expansion

$$v(x,\tau,\omega) = \overline{v}(x,\tau) + \sum_{i=1}^{\infty} \Theta_i(\tau,\omega) v_i(x,\tau), \tag{1}$$

where $\overline{v}(x,\tau)$ is the expected value function, $\Theta_i(\tau,\omega)$ are zero-mean stochastic processes, and $v_i(x,\tau)$ are linearly independent fields in physical space, with $\{\Theta_i\}$, $\{v_i\}$ possibly orthonormal bases in random and physical space, respectively. The scaled time τ is a function of physical time that we may also allow to be stochastic, i.e., $\tau = \tau(t,\omega)$. Eq. (1) is a generalization of the classical Karhunen-Loève expansion with time dependent stochastic and deterministic components. Several methods can be derived by substituting the expansion (1) into the nonlinear model of interest. In all subsequent examples we will assume that the stochastic dimensionality can be restricted to n dominant dimensions of uncertainty. The temporal evolution of the basis $\{v_i\}$ is restricted to the instantaneous normal direction, i.e., any new contribution is orthogonal to the current basis. By projecting the governing PDE onto the bases $\{\Theta_i\}$ and $\{v_i\}$ while keeping $\tau = t$ fixed, one obtains the Dynamically Orthogonal (DO) field equations [40,41]. The DO method was used to solve the stochastic Navier–Stokes equations in Sapsis and Lermusiaux [42]. Employing a linear scaling of τ with respect to time t in connection with the Dual DO equations (where the stochastic instead of the deterministic basis is kept orthonormal) led to improvement in the performance by means of smaller effective number of terms in (1) [43]. By fixing the stochastic basis with respect to time and letting $\Theta_i(\omega) = \Psi_i(\boldsymbol{\xi}(\theta))$ be orthogonal polynomials with respect to some choice of random vector $\boldsymbol{\xi}(\theta)$, the DO field equations reduce to the stochastic Galerkin projection of the gPC expansion. Controlling the dynamics of $\tau(\boldsymbol{\xi},t)$ with an ODE results in the ATI method. Next, we will describe gPC and ATI in some more detail.

2.1. Generalized polynomial chaos

gPC offers a framework by spectral expansions in random variables via orthogonal, stochastic polynomials. Assume that all input random variables and fields of relevance to the application of interest can be parameterized to sufficient accuracy by an n-dimensional random vector $\boldsymbol{\xi} = (\xi_1, \ldots, \xi_n)$, where for brevity of notation we have omitted the dependence on Ω, i.e., $\boldsymbol{\xi} = \boldsymbol{\xi}(\omega)$. The random variables are assumed independent with joint PDF $w(\boldsymbol{\xi}) = w_1(\xi_1)\ldots w_n(\xi_n)$.

Let $\{\Psi_{\boldsymbol{i}}(\boldsymbol{\xi})\}$ be a set of normalized multivariate polynomials orthogonal with respect to w, where $\boldsymbol{i} = (i_1, \ldots, i_n) \in \mathbb{N}_0^n$. The multivariate polynomials are products of univariate Wiener-Askey polynomials, i.e., $\Psi_{\boldsymbol{i}}(\boldsymbol{\xi}) = \psi_{i_1}(\xi_1)\ldots\psi_{i_n}(\xi_n)$. The orthogonality of polynomials implies that

$$\mathbb{E}_{\boldsymbol{\xi}}\big(\Psi_{\boldsymbol{i}}(\boldsymbol{\xi})\Psi_{\boldsymbol{j}}(\boldsymbol{\xi})\big) = \prod_{k=1}^{n} \delta_{i_k j_k}, \quad i_k, j_k \in \mathbb{N}_0, \tag{2}$$

where δ_{ij} is the Kronecker delta and $\mathbb{E}_{\boldsymbol{\xi}}(\cdot)$ denotes the expectation operator,

$$\mathbb{E}_{\boldsymbol{\xi}}(f) = \int f(\boldsymbol{\xi}) w(\boldsymbol{\xi}) \mathrm{d}\boldsymbol{\xi}. \tag{3}$$

Any finite-variance random field $x(\boldsymbol{\xi})$ can then be expressed by its gPC expansion,

$$x(\boldsymbol{\xi}) = \sum_{\boldsymbol{i}\in\mathbb{N}_0} x_{\boldsymbol{i}} \Psi_{\boldsymbol{i}}(\boldsymbol{\xi}). \tag{4}$$

For practical use, the gPC expansion must be truncated to a finite number of terms by restricting the order of the polynomials. The truncation scheme is defined by selecting a finite index set $\mathcal{I} \subset \mathbb{R}_0^n$ given by

$$\mathcal{I} = \{\mathbf{i} \in \mathbb{R}_0^n : \|\mathbf{i}\|_q \le p\}, \tag{5}$$

where the q-norm (or quasi-norm if $q < 1$) is defined by

$$\|\mathbf{i}\|_q = \left(\sum_{j=1}^{n} i_j^q\right)^{1/q}. \tag{6}$$

Setting $q = 1$ leads to the total-order truncation including all powers up to p, which is used in this work. Choosing $q < 1$ yields the hyperbolic index sets [11], favoring the influence of univariate polynomials at the expense of high-order mixed polynomials including several random dimensions. Other options include the hyperbolic cross truncation strategy where compound nonlinear effects from multiple random variables are truncated in favor of higher-order nonlinear effects in single and small numbers of joint variables [44]. The total number of terms $(P+1)$ in an isotropic total-order expansion of maximum polynomial order p and n uncertain input variables is given by

$$P + 1 = \frac{(n+p)!}{n!\,p!}. \tag{7}$$

Using single-index notation, i.e., mapping the vector-valued multi-index set to the non-negative integers, the resulting scalar indices correspond to different multi-dimensional basis functions. The truncated gPC expansion then reads

$$x(\boldsymbol{\xi}) \approx \sum_{i=0}^{P} x_i \Psi_i(\boldsymbol{\xi}). \tag{8}$$

Once the truncated gPC coefficients in (4) are calculated, the expected value $\mathbb{E}_{\boldsymbol{\xi}}(x)$ and the approximate variance $\mathbb{V}_{\boldsymbol{\xi}}(x)$ of the stochastic solution are given by

$$\mathbb{E}_{\boldsymbol{\xi}}(x) = x_0,$$
$$\mathbb{V}_{\boldsymbol{\xi}}(x) = \sum_{i=1}^{P} x_i^2.$$

3. Asynchronous time integration

Generalized polynomial chaos fails to represent periodic QoIs that are characterized by a stochastic frequency. To overcome this problem, Le Maître et al. introduced asynchronous time integration (ATI) [35]. We will briefly describe the method in the following. For a more detailed explanation, the reader is referred to [35]. Consider a set of stochastic ODEs, written as

$$\frac{d}{dt}\boldsymbol{y}(\boldsymbol{\xi},t) = \mathcal{F}(\boldsymbol{y}(\boldsymbol{\xi},t)), \tag{9}$$

where $\boldsymbol{y}(\boldsymbol{\xi},t)$ is a random vector and $\mathcal{F}$ is a discrete operator. Now choose a certain realization of $\boldsymbol{\xi}$ as a deterministic reference and call this solution $\boldsymbol{y}^{(r)}$ that obeys Eq. (9):

$$\frac{d}{dt}\boldsymbol{y}^{(r)}(t) = \mathcal{F}^{(r)}(\boldsymbol{y}^{(r)}(t)). \tag{10}$$

Eqs. (9) and (10) can be seen as semi-discretized PDEs, where the vector $\boldsymbol{y}$ will later be assigned to the gPC expanded velocity components. Building on this, $\mathcal{F}$ can be interpreted as an operator that describes the convection, diffusion and the pressure term included in the Navier–Stokes equations.

The focus on the incompressible Navier–Stokes equations makes our work differ from [35], where small systems of ODEs were considered. For almost all $\boldsymbol{\xi}$, Eq. (9) is satisfied by solutions $\boldsymbol{y}(\boldsymbol{\xi},t)$,

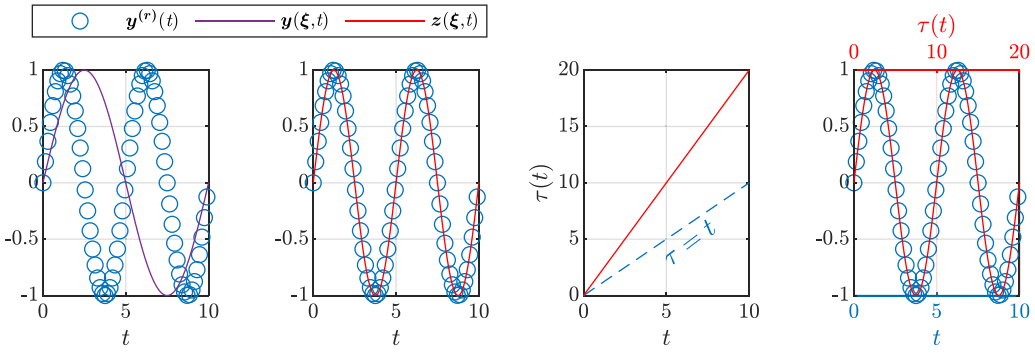

Fig. 1. The behavior of the stochastic solution $\boldsymbol{y}(\boldsymbol{\xi},t)$ and the in-phase solution $\boldsymbol{z}(\boldsymbol{\xi},t)$ in the t- and τ-time space.

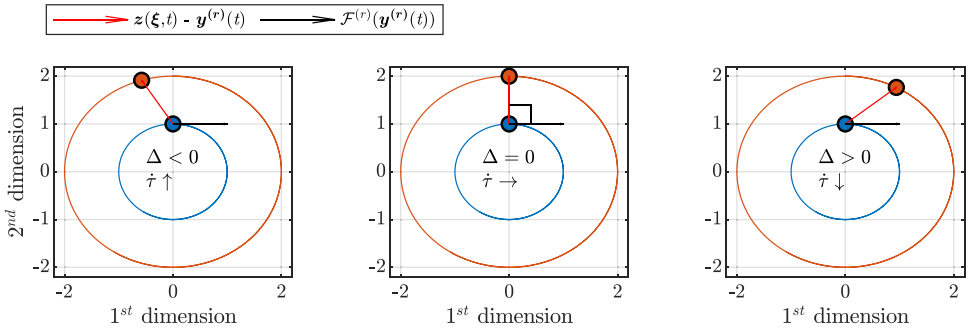

Fig. 2. Phase portrait of a realization of the stochastic solutions $\boldsymbol{z}(\boldsymbol{\xi},t)$ (orange) and the reference $\boldsymbol{y}^{(r)}$ (blue), where $\boldsymbol{y}^{(r)},\boldsymbol{z}:\mathbb{R}^n\to\mathbb{R}^2$. The vectors represent the input for $\Delta=\boldsymbol{d}(\boldsymbol{\xi},t)\cdot\mathcal{F}^{(r)}(\boldsymbol{y}^{(r)}(t))$. (For interpretation of the references to color in this figure legend, the reader is referred to the web version of this article.)

each associated with a particular oscillation frequency $f(\boldsymbol{\xi})$. This frequency is slightly shifted from a reference frequency $f^{(r)}$ that corresponds to a reference solution $\boldsymbol{y}^{(r)}$. We now stretch and compress the solutions $\boldsymbol{y}(\boldsymbol{\xi},t)$ so that all signals have the same frequency $f^{(r)}$. We call these uniformly oscillating solutions $\boldsymbol{z}(\boldsymbol{\xi},t)$, which can be generated by introducing a stochastic time variable $\tau(\boldsymbol{\xi},t)$ that is a function of the physical time t and of the random realization $\boldsymbol{\xi}$ (i.e., the time rescaling is different for each realization):

$$\boldsymbol{z}(\boldsymbol{\xi},t)=\boldsymbol{y}(\boldsymbol{\xi},\tau(\boldsymbol{\xi},t)). \tag{11}$$

In order to get a formulation for the uniformly oscillating solutions $\boldsymbol{z}(\boldsymbol{\xi},t)$ on the basis of the operator $\mathcal{F}$, the chain rule is applied to Eq. (11):

$$\frac{d}{dt}\boldsymbol{z}(\boldsymbol{\xi},t)=\frac{d}{dt}\boldsymbol{y}(\boldsymbol{\xi},t)\Big|_{t=\tau(\boldsymbol{\xi},t)}\frac{d\tau}{dt}=\mathcal{F}(\boldsymbol{y}(\boldsymbol{\xi},\tau(\boldsymbol{\xi},t)))\dot{\tau}=\mathcal{F}(\boldsymbol{z}(\boldsymbol{\xi},t))\dot{\tau}. \tag{12}$$

The term $\mathcal{F}(\boldsymbol{z}(\boldsymbol{\xi},t))\dot{\tau}$ is a scaled version of $\mathcal{F}(\boldsymbol{z}(\boldsymbol{\xi},t))$, which guarantees that the solutions $\boldsymbol{z}(\boldsymbol{\xi},t)$ are in phase.

Fig. 1 illustrates the process of the time transformation. From left to right: (1) The reference solution and a solution $\boldsymbol{y}(\boldsymbol{\xi},t)$ of a selected realization of $\boldsymbol{\xi}$ are shown, which are out of phase. (2) Using a time scaling, it is possible to align both signals by choosing $\boldsymbol{z}(\boldsymbol{\xi},t)$ so that they are in phase in the t-time space. (3) Since the reference solution has double the frequency compared to $\boldsymbol{y}(\boldsymbol{\xi},t)$ in this example $\tau(t)=2t$. (4) To retrieve $\boldsymbol{y}(\boldsymbol{\xi},t)$, we plot $\boldsymbol{z}(\boldsymbol{\xi},t)$ over $\tau(t)$. The signals appear to be in phase, but the τ-axis progresses twice as fast. Therefore, the original frequency of $\boldsymbol{y}(\boldsymbol{\xi},t)$ is restored in the τ-time space.

The time scaling can be summarized as

$$\begin{cases}\boldsymbol{z}(\boldsymbol{\xi},t)=\boldsymbol{y}(\boldsymbol{\xi},\tau(\boldsymbol{\xi},t)) & \text{(push-forward)},\\ \boldsymbol{y}(\boldsymbol{\xi},t)=\boldsymbol{z}(\boldsymbol{\xi},\tau^{-1}(t,\boldsymbol{\xi})) & \text{(pull-backward)},\end{cases} \tag{13}$$

where the push-forward operation describes the process in which all solutions are brought into phase. The pull-backward time scaling is used to recover the original oscillatory behavior of the solution. The task now is to find a way of describing τ that guarantees in-phase behavior between the solutions $\boldsymbol{z}(\boldsymbol{\xi},t)$ and the reference solution $\boldsymbol{y}^{(r)}$.

The distance between the stochastic solution and the reference solution in the phase portrait can be expressed as

$$\boldsymbol{d}(\boldsymbol{\xi},t)=\boldsymbol{z}(\boldsymbol{\xi},t)-\boldsymbol{y}^{(r)}(t). \tag{14}$$

When the distance vector and the velocity vector of the reference trajectory are orthogonal, the solutions oscillate in phase. The following dot product is therefore a measure of their phase shift:

$$\Delta=\boldsymbol{d}(\boldsymbol{\xi},t)\cdot\mathcal{F}^{(r)}(\boldsymbol{y}^{(r)}(t)). \tag{15}$$

This relation is graphically shown in Fig. 2, where $\boldsymbol{z}(\boldsymbol{\xi},t)$ and $\boldsymbol{y}^{(r)}$ are two-dimensional vectors. When the trajectories are in phase (middle), then $\Delta=0$ and the clock speed does not need to be adjusted. If $\Delta<0$ (left), the local clock speed must be increased so that the stochastic trajectory can catch up with the reference solution and vice versa (right).

Le Maître et al. [35] proposed an ODE for the determination of $\dot{\tau}$ that enforces the $\Delta=0$ criterion:

$$\frac{d}{dt}\dot{\tau}(\boldsymbol{\xi},t)=-\alpha_0\dot{\tau}(\boldsymbol{\xi},t)\Delta(\boldsymbol{\xi},t)+\alpha_1(1-\dot{\tau}(\boldsymbol{\xi},t)). \tag{16}$$

In this expression α_0 determines how fast the local clock speed responds to changes in $\Delta(\boldsymbol{\xi},t)$, α_1 controls the asymptotic behavior of $\dot{\tau}$, and $(1-\dot{\tau})$ ensures that the clock speed remains close to 1. Additionally, these parameters are chosen in a way that the fixed point $\dot{\tau}^*$, i.e., the value of $\dot{\tau}$ that makes the right-hand-side of Eq. (16) equal to zero or equivalently $\frac{d}{dt}\dot{\tau}=0$, should behave as an attractor for a large range of Δ. Consequently, the dynamical adjustment of the clock speed as illustrated in Fig. 2 is assured. We summarize the system of equations that follow the ATI method:

$$\frac{d}{dt}\boldsymbol{y}^{(r)}(t)=\mathcal{F}^{(r)}(\boldsymbol{y}^{(r)}(t)), \tag{17}$$

$$\frac{d}{dt}\boldsymbol{z}(\boldsymbol{\xi},t) = \dot{\tau}\mathcal{F}(\boldsymbol{z}(\boldsymbol{\xi},t)), \tag{18}$$

$$\frac{d}{dt}\dot{\tau}(\boldsymbol{\xi},t) = -\alpha_0\dot{\tau}(\boldsymbol{\xi},t)\Delta(\boldsymbol{\xi},t) + \alpha_1(1-\dot{\tau}(\boldsymbol{\xi},t)), \tag{19}$$

with initial conditions:

$$\boldsymbol{y}^{(r)}(t=0) = \boldsymbol{y}^0, \tag{20}$$

$$\boldsymbol{z}(\boldsymbol{\xi}, t=0) = \boldsymbol{y}^0, \tag{21}$$

$$\dot{\tau}(\boldsymbol{\xi}, t=0) = 1. \tag{22}$$

In all numerical experiments we set $\alpha_0 = 8e{-}5$ and $\alpha_1 = 10$.

Note that no exact knowledge of the functional dependence of t and τ is required when following the ATI method as the dynamics of $\dot{\tau}$ is controlled via an ODE. Accordingly, we consider the ATI approach to be more general if compared to other methods, as the one followed in Musharbash and Nobile [43], where an explicit algebraic relation between t and τ is required. Next, we will apply the ATI framework to the incompressible Navier–Stokes equations.

4. Application to the incompressible Navier–Stokes equations

4.1. Stochastic flow formulation

The Navier–Stokes equations are obtained from conservation laws of mass and momentum. In case of incompressible flows, the density is assumed to be constant in space and time. Conservation of mass and momentum reduce to:

$$\nabla\cdot\boldsymbol{u} = 0, \tag{23}$$

$$\frac{\partial\boldsymbol{u}}{\partial t} + (\boldsymbol{u}\cdot\nabla)\boldsymbol{u} = -\frac{1}{\rho}\nabla p + \nu\nabla^2\boldsymbol{u}, \tag{24}$$

with suitable boundary conditions to be described later, and where $\boldsymbol{u}$, p, ρ and ν represent the velocity, pressure, density, and the kinematic viscosity, respectively. In this study we assume that $\boldsymbol{u}$, p and ν are stochastic. Therefore, these quantities are expanded as gPC series (8) and inserted into the governing equations, which yields

$$\sum_{i=0}^{P}\Psi_i\nabla\cdot\boldsymbol{u}_i = 0, \tag{25}$$

$$\sum_{i=0}^{P}\Psi_i\frac{\partial\boldsymbol{u}_i}{\partial t} + \sum_{i=0}^{P}\sum_{j=0}^{P}\Psi_i\Psi_j(\boldsymbol{u}_i\cdot\nabla)\boldsymbol{u}_j = -\sum_{i=0}^{P}\Psi_i\frac{1}{\rho}\nabla p_i + \sum_{i=0}^{P}\sum_{j=0}^{P}\Psi_i\Psi_j\nu_i\nabla^2\boldsymbol{u}_j \tag{26}$$

The system Eqs. (25) and (26) is projected onto the stochastic basis $\{\Psi_k\}$, which is composed by orthonormal polynomials (see Eq. (2)). This results in $P+1$ equations for mass conservation and $3(P+1)$ equations for momentum conservation:

$$\nabla\cdot\boldsymbol{u}_k = 0, \tag{27}$$

$$\frac{\partial\boldsymbol{u}_k}{\partial t} + \sum_{i=0}^{P}\sum_{j=0}^{P}\mathbb{E}_{\boldsymbol{\xi}}\big(\Psi_i\Psi_j\Psi_k\big)(\boldsymbol{u}_i\cdot\nabla)\boldsymbol{u}_j = -\frac{1}{\rho}\nabla p_k + \sum_{i=0}^{P}\sum_{j=0}^{P}\mathbb{E}_{\boldsymbol{\xi}}\big(\Psi_i\Psi_j\Psi_k\big)\nu_i\nabla^2\boldsymbol{u}_j, \tag{28}$$

where $k = 0,\dots,P$. The expectations of basis function triples $\mathbb{E}_{\boldsymbol{\xi}}\big(\Psi_i\Psi_j\Psi_k\big)$ can be computed exactly for orthogonal polynomials using Gaussian quadrature rules. Alternatively, closed-form expressions for some families of expectations of triple products based on polynomial recurrence relations are available in the literature [45]. The numerical method used to solve the stochastic, incompressible Navier–Stokes equations is presented in Appendix A.

4.2. Asynchronous time integration of incompressible Navier–Stokes

We define $\mathcal{F}$ as a discrete operator associated with the stochastic momentum equation

$$\mathcal{F}(\boldsymbol{u}(\boldsymbol{\xi},t)) = \Big[-\Big(\boldsymbol{u}(\boldsymbol{\xi},t)\cdot\nabla\Big)\boldsymbol{u}(\boldsymbol{\xi},t) - \frac{1}{\rho}\nabla p(\boldsymbol{\xi},t) + \nu(\boldsymbol{\xi})\nabla^2\boldsymbol{u}(\boldsymbol{\xi},t)\Big], \tag{29}$$

where the brackets '[ ]' symbolize the spatial discretization operation. In a similar way, $\mathcal{F}^{(r)}$ is defined as a discrete operator associated with the deterministic momentum equation

$$\mathcal{F}^{(r)}(\boldsymbol{u}^{(r)}(t)) = \Big[-\Big(\boldsymbol{u}^{(r)}\cdot\nabla\Big)\boldsymbol{u}^{(r)} - \frac{1}{\rho}\nabla p^{(r)} + \nu^{(r)}\nabla^2\boldsymbol{u}^{(r)}\Big]. \tag{30}$$

Eq. (18) is rewritten resulting in

$$\frac{d}{dt}\boldsymbol{u}(\boldsymbol{\xi},t) = \dot{\tau}(\boldsymbol{\xi})\mathcal{F}(\boldsymbol{u}(\boldsymbol{\xi},t)). \tag{31}$$

Applying gPC expansion to Eq. (31) and projecting the resulting expression on the stochastic polynomial basis leads to

$$\frac{d}{dt}\boldsymbol{u}_k = \mathcal{F}_k^{\mathrm{gPC}}, \quad \text{for } k = 0,\dots,P, \tag{32}$$

where $\dot{\tau}(\boldsymbol{\xi})$ has been incorporated in the operator $\mathcal{F}_k^{\mathrm{gPC}}$:

$$\mathcal{F}_k^{\mathrm{gPC}} = \Bigg[-\sum_{i=0}^{P}\sum_{j=0}^{P}\sum_{m=0}^{P}\mathbb{E}_{\boldsymbol{\xi}}\big(\Psi_i\Psi_j\Psi_m\Psi_k\big)\dot{\tau}_i(\boldsymbol{u}_j\cdot\nabla)\boldsymbol{u}_m - \sum_{i=0}^{P}\sum_{j=0}^{P}\mathbb{E}_{\boldsymbol{\xi}}\big(\Psi_i\Psi_j\Psi_k\big)\dot{\tau}_i\frac{1}{\rho}\nabla p_j\Bigg] \tag{33}$$

$$+\Bigg[\sum_{i=0}^{P}\sum_{j=0}^{P}\sum_{m=0}^{P}\mathbb{E}_{\boldsymbol{\xi}}\big(\Psi_i\Psi_j\Psi_m\Psi_k\big)\dot{\tau}_i\nu_j\nabla^2\boldsymbol{u}_m\Bigg]. \tag{33}$$

In a similar way, Eq. (19) is expanded leading to a system of ODEs for the coefficient $\dot{\tau}_k$, as shown in Appendix B. Note that the expectations of the quadruple product $\mathbb{E}_{\boldsymbol{\xi}}\big(\Psi_i\Psi_j\Psi_m\Psi_k\big)$ are calculated using Gaussian quadrature rules.

5. Statistical quantities of interest

Numerical simulation of unsteady periodic flow permits a detailed investigation of the system as a result of the large amount of information: temporal signals for each flow variable at every node of the computational domain. Aside from the instantaneous fields obtained by the simulation, two statistical quantities are generally of major interest in studies featuring instability, vibrations and/or limit cycles: the temporal expected value $\mathbb{E}_t(\boldsymbol{y}(t))$, and the temporal variance $\mathbb{V}_t(\boldsymbol{y}(t))$. A schematic representation of a signal $y(t)$, associated with a given point in physical space of the field $\boldsymbol{y}(t)$, is given in Fig. 3 (gray curve).

For illustration purposes, we discretize the field $\boldsymbol{y}(\boldsymbol{\xi},t)$ in random space by N different realizations, as depicted in Fig. 3 (red curves), along with the PDFs of $\mathbb{E}_t\big(\boldsymbol{y}(\boldsymbol{\xi},t)\big)$ and $\mathbb{V}_t\big(\boldsymbol{y}(\boldsymbol{\xi},t)\big)$. To quantify the behavior of a given periodic, stochastic field $\boldsymbol{y}(\boldsymbol{\xi},t)$ it is convenient to define four measures:

$$\mathbb{EE} \equiv \mathbb{E}_{\boldsymbol{\xi}}(\mathbb{E}_t(\boldsymbol{y})) = \mathbb{E}_t\big(\mathbb{E}_{\boldsymbol{\xi}}(\boldsymbol{y})\big) = \bar{\boldsymbol{y}}_0, \tag{34}$$

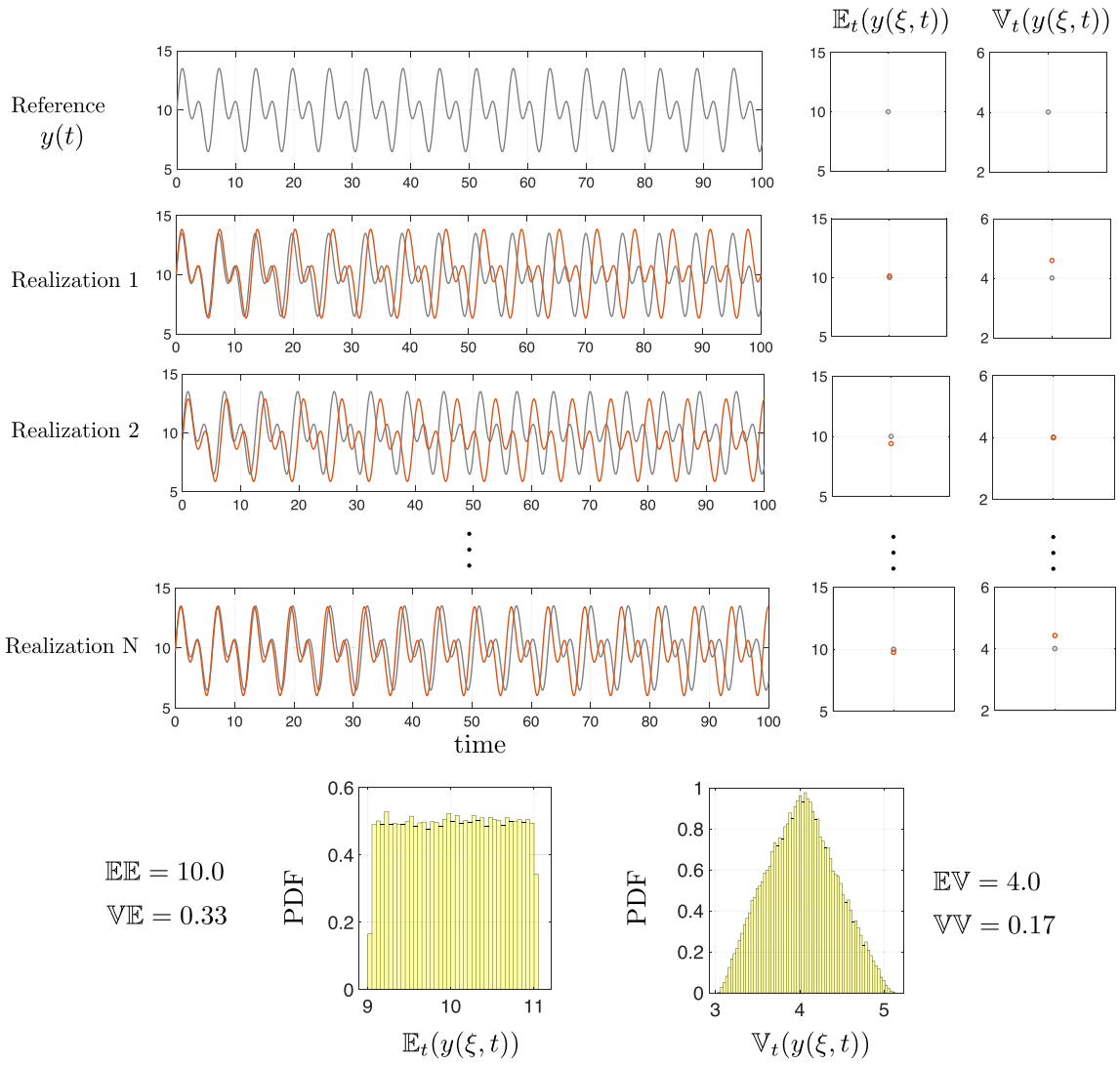

Fig. 3. Illustration of signal $y(\xi, t)$ for N realizations. The signal is characterized by four scalars $\mathbb{EE}$, $\mathbb{VE}$, $\mathbb{EV}$ and $\mathbb{VV}$.

$$\mathbb{EV} \equiv \mathbb{E}_{\boldsymbol{\xi}}(\mathbb{V}_t(\boldsymbol{y})) = \sum_{i=0}^{P} \mathbb{E}_t \boldsymbol{y}_i^2 - (\mathbb{E}_t \boldsymbol{y}_i)^2 = \sum_{i=0}^{P} \overline{\boldsymbol{y}_i^2} - \bar{\boldsymbol{y}}_i^2, \tag{35}$$

$$\mathbb{VE} \equiv \mathbb{V}_{\boldsymbol{\xi}}(\mathbb{E}_t(\boldsymbol{y})) = \sum_{i=0}^{P} \bar{\boldsymbol{y}}_i^2, \tag{36}$$

$$\begin{aligned}\mathbb{VV} \equiv \mathbb{V}_{\boldsymbol{\xi}}(\mathbb{V}_t(\boldsymbol{y})) &= \sum_{m=1}^{2P} \left(\sum_{i=0}^{P} \sum_{j=0}^{P} \left(\overline{\boldsymbol{y}_i \boldsymbol{y}_j} - \overline{\boldsymbol{y}_i}\ \overline{\boldsymbol{y}_j}\right) \mathbb{E}_{\boldsymbol{\xi}}(\Psi_i \Psi_j \Psi_k) \right)^2 \\ &\neq \sum_{i=0}^{P} \sum_{j=0}^{P} \overline{\boldsymbol{y}_i^2 \boldsymbol{y}_j^2} - \overline{\boldsymbol{y}_i^2}\ \overline{\boldsymbol{y}_j^2} = \mathbb{V}_t\left(\mathbb{V}_{\boldsymbol{\xi}}(\boldsymbol{y})\right),\end{aligned} \tag{37}$$

where the bar notation $\bar{\boldsymbol{y}}$ has been temporarily introduced to facilitate to distinguish between temporal and stochastic mean values.

These expressions are the expected value in random space of the temporal mean (Eq. (34)) and variance (Eq. (35)), respectively, as well as the variance of the same temporal mean Eq. (36) and variances Eq. (37). The latter two can be used to define error bars for the two former expectations. In the example of Fig. 3, we observe in the histogram plot at the bottom left that the temporal mean value of each signal varies considerably along realizations ($9 < \mathbb{E}_t(\boldsymbol{y}(\boldsymbol{\xi}, t)) < 11$). We also observe variability in the temporal variance ($3 < \mathbb{V}_t(\boldsymbol{y}(\boldsymbol{\xi}, t)) < 5$).

The quantities $\mathbb{EE}$, $\mathbb{EV}$, $\mathbb{VE}$ and $\mathbb{VV}$ are useful when assessing how the temporal mean and temporal variance of a periodic flow is affected by input uncertainties. If only those measures are of interest, NigPC should be the method considered, as it is easy to implement and performs satisfactorily. Note that the shape of limit cycle signals, described by k characteristic amplitudes (period-k limit cycles) and frequencies, are not captured by $\mathbb{EE}$, $\mathbb{EV}$, $\mathbb{VE}$ and $\mathbb{VV}$. Such information can be, nevertheless, of high interest in cases, e.g. when the frequency content of the signals and maxima of the corresponding crests are required. Accordingly, in the study of flow limit cycles, it is generally appropriate to analyze the signals directly, e.g. by building phase portraits of correlated quantities. It might also be of interest to evaluate the probability distribution that characterizes a periodic flow variable. For such requirements, the quantities $\mathbb{EE}$, $\mathbb{EV}$, $\mathbb{VE}$ and $\mathbb{VV}$ are not suited. In this work, we show that an adequate surrogate model for $\boldsymbol{y}(\boldsymbol{\xi}, t)$ is feasible by means of igPC (standard or ATI) for oscillating laminar flows.

6. Numerical results

The implementation of the method (Section 4) in our in-house solver is validated in the supplementary material using a back-

Table 1
Numerical values of characteristic length scales.

H/h_c	B/h_c	L_u/h_c	L_d/h_c	b_c/h_c	Grid-size
8	16	3.5	10.5	2	80×160

Table 2
Coordinates of the probes.

	P①	P②	P③	P④	P⑤	P⑥
x/h_c	3.5	5.3	7.1	3.5	5.3	7.1
y/h_c	0	0	0	2.5	2.5	2.5

ward facing step. The resulting tool is named SUN-S (**S**tochastic **U**nsteady **N**avier–**S**tokes) and can take into account uncertainties in the fluid viscosity and in boundary conditions for velocity $\boldsymbol{u}$ and pressure p. It was developed for MATLAB 2017b based on finite volumes. The numerical test cases are one-dimensional in stochastic space. The extension to multiple dimensions is conceptually straightforward but leads to increased computational cost, as discussed in more detail in Section 6.4.

6.1. Flow around a rectangular cylinder

We investigate the Kármán vortex street generated by a rectangular cylinder. The vortex shedding downstream the interfering body is a well-known observation in fluid mechanics. Vortices are formed at the back of the cylinder and periodically separate from the upper and lower side of the body. Although the phenomenon is associated with Kármán's name, the first experimental observations were reported by Mallock [46] and Bénard [47] in 1907 and 1908. The main contribution of Kármán was the stability analysis of the vortex formation and the explanation of the mechanisms of wake drag in 1911 [48]. The Kármán vortex street is an interesting problem because we observe unsteady quantities while the flow pattern can still be assigned to the laminar regime. Therefore, we can solve the original Navier–Stokes equations without further turbulence modeling.

The geometry and the relevant dimensions are shown in Fig. 4. Table 1 presents the associated numerical values. The coordinates of the probes are listed in Table 2. The inlet velocity describes a flat profile with the bulk velocity u_{in}. The pressure gradient at the inlet is zero. On the top and bottom boundaries of the domain we set a zero gradient condition for both velocity and pressure. The

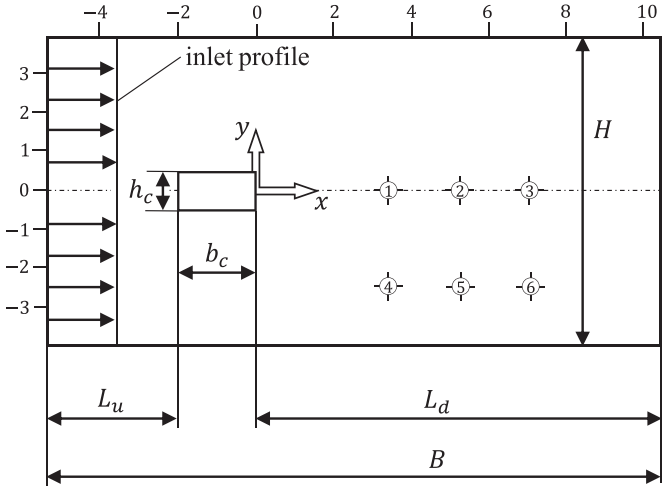

Fig. 4. Geometry, length scales and location of the probes of a 2D flow with a rectangular bluff body.

outflow boundary conditions are as follows:

$$\frac{\partial u}{\partial x} = 0, \quad \frac{\partial v}{\partial y} = 0 \quad \text{and} \quad p = 1 \text{ atm}. \tag{38}$$

The rectangular cylinder is placed on the line of symmetry with respect to the height H and its surfaces are modeled as solid, non-slip walls. The Reynolds number for this specific case is given by

$$Re = \frac{u_{in} \cdot h_c}{\nu}, \tag{39}$$

where ν is the kinematic viscosity and h_c is the height of the cylinder.

We study two cases and consider an artificial fluid. Case A refers to variations of kinematic viscosity, and case B refers to variations of inlet velocity. Both cases correspond to the same range in $Re \in [95,105]$. Fig. 5 (left) shows the characteristic frequency of the wake oscillation as a function of the Strouhal number $Sr = f \cdot h_c/u_{in}$. Probe ⑤ is used to measure the oscillations. Results, which are in agreement with [49–52] are scattered along one single line around $Sr \approx 0.135$.

Fig. 5 (right) shows the oscillation frequency for the same cases. Changes in Re lead to stronger frequency variations in Case B. Case A exhibits almost no change in frequency in the range $Re \in [70, 130]$.

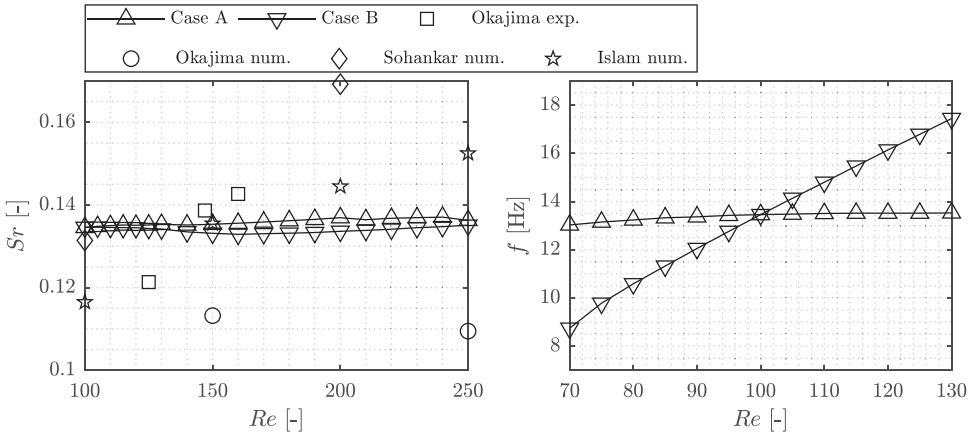

Fig. 5. Strouhal number as a function of Reynolds number for $b_c/h_c = 2$ (left). Results are shown in the range $Re \in [100, 250]$ for comparison with other studies (Okajima exp. [49], Okajima num. [50], Sohankar num. [51] and Islam num. [52]). Frequency of the oscillations in the wake of the cylinder as a function of Re (right). Results are shown in the range $Re \in [70, 130]$.

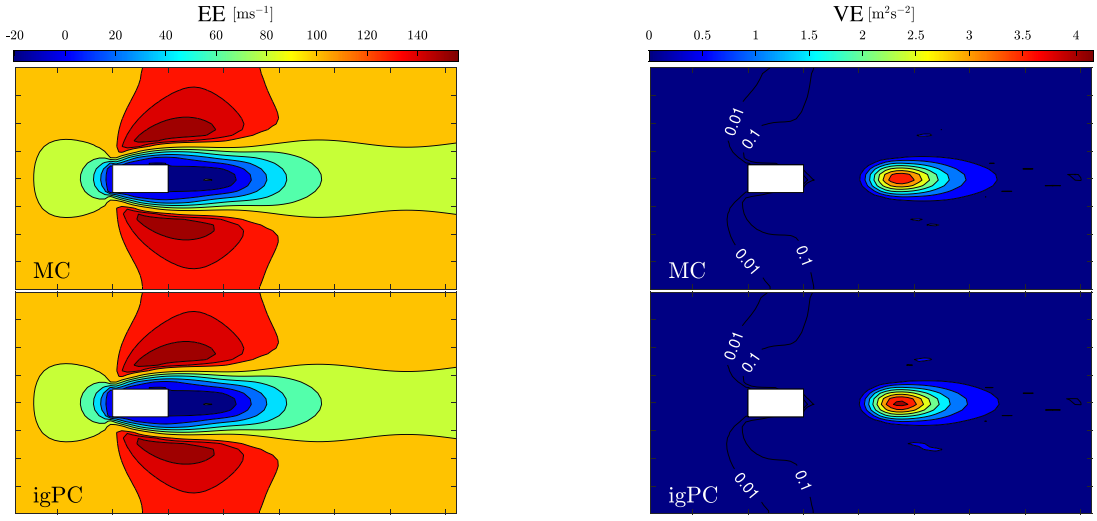

Fig. 6. Fields $\mathbb{EE}$ and $\mathbb{VE}$ for case A.

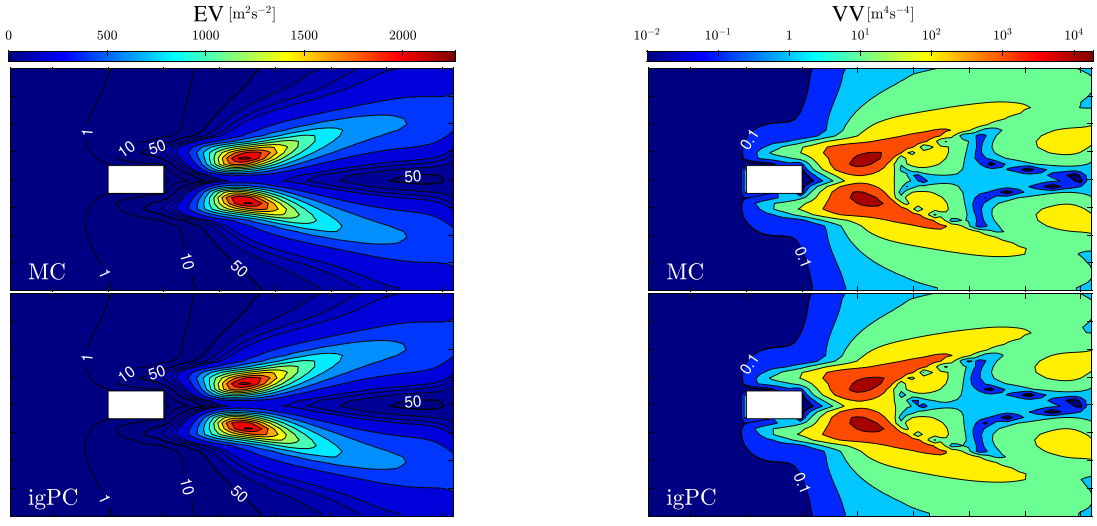

Fig. 7. Fields $\mathbb{EV}$ and $\mathbb{VV}$ for case A.

6.2. Case A: uncertain viscosity

In this section, we consider the kinematic viscosity to be uncertain:

$$\nu(\xi) = \nu_0 + \nu_1 \xi, \tag{40}$$

where $\xi \sim U[-1, 1]$ is a uniform distribution and $\nu_0 = 1$ m^2 s^{-1}, and $\nu_1 = 0.052$ m^2 s^{-1}. The inlet velocity is deterministic and constant with a value 100 ms^{-1}. Consequently, $Re \in [95, 105]$. We consider normalized Legendre polynomials for gPC.

The simulation is carried out using the standard intrusive gPC technique (not ATI) and the results are validated in three different ways.

i) The fields associated with $\mathbb{EE}$, $\mathbb{VE}$, $\mathbb{EV}$ $\mathbb{VV}$, introduced in Section 5, are compared to the fields obtained from the Monte Carlo simulation.
ii) Three realizations of ξ are selected and corresponding values of velocity are computed from the gPC model (8). Results are compared in a phase portrait to velocity time series obtained from three different deterministic simulations.
iii) A Monte Carlo simulation is performed with 500 samples. The corresponding PDF at two locations and three time instants are compared to the ones obtained from the gPC simulation.

Figs. 6 and 7 show the fields of $\mathbb{EE}$, $\mathbb{VE}$, $\mathbb{EV}$ and $\mathbb{VV}$ calculated from established limit cycles. We observe that $\mathbb{EE}$ captures the recirculation zone (dark blue) dowsntream of the bluff-body. The field of $\mathbb{EV}$ (Fig. 7) suggests that this recirculation zone does not exhibit oscillations in the region immediately downstrem of the rectangular cylinder, as indicated by the dark blue zone of $\mathbb{EV}$. As expected, a large region of constant inlet velocity (no oscillations) is encountered upstream of the bluff-body. The field $\mathbb{EE}$ also shows regions where the temporal mean velocity is high (dark red). Note that only a portion of this region exhibits oscillations of small amplitude. The field $\mathbb{EV}$ shows zones where the amplitude of the oscillations is high, as observed in the two symmetric dark red zones. We also observe two elongated, symmetric areas downstream of the bluff-body. These regions characterize the increasing/decreasing amplitude of the wake downstream of the rectangular cylinder.

The field $\mathbb{VE}$ suggests that the temporal mean value of the oscillations ($\mathbb{E}_t$) is not strongly influenced by uncertainties of ν over large regions. The oval shape area depicted in red is the only predominant region, where the temporal mean of velocity oscillations is affected by uncertainties in ν. The field $\mathbb{VV}$ shows the influence of ν uncertainties on the amplitude of oscillations of velocity. The variability is confined within the red-colored region of $\mathbb{EV}$, which

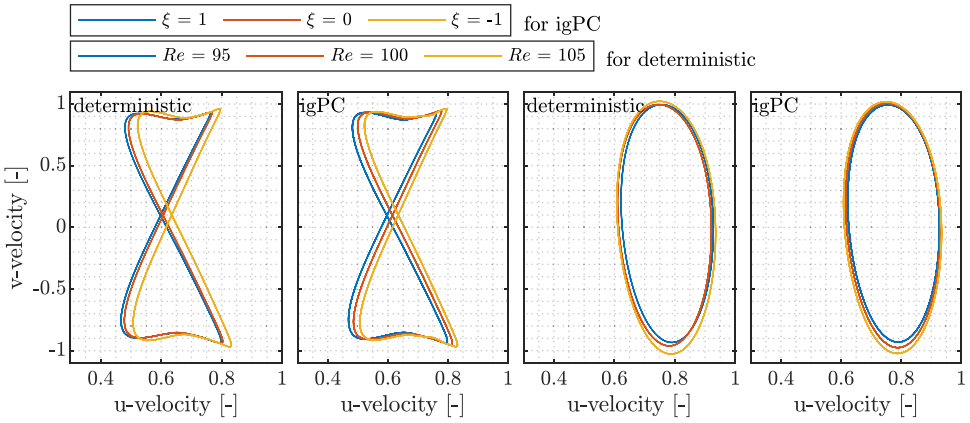

Fig. 8. Limit cycle oscillations for probe ② (left, period-two limit cycles) and probe ⑤ (right, period-one limit cycles) of the reference and the stochastic simulation with $P = 4$ for different realizations of ξ.

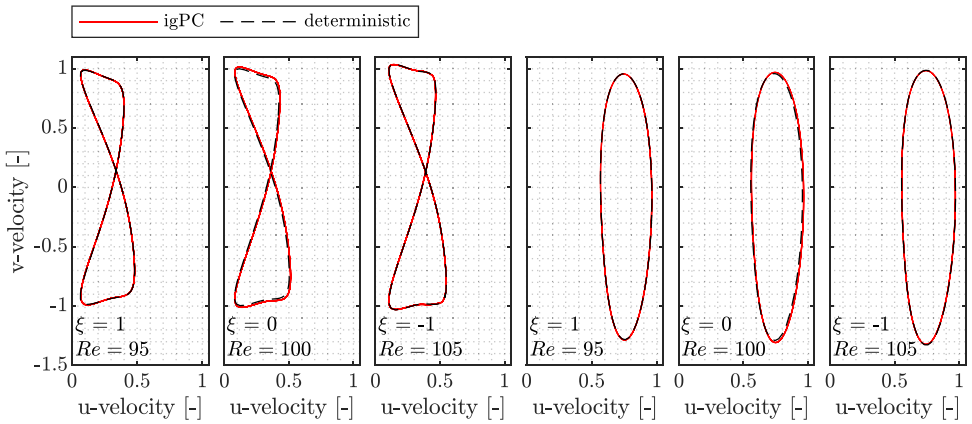

Fig. 9. Limit cycle oscillations for probe ① (left) and probe ⑥ (right) of the reference and the corresponding stochastic simulation with $P = 4$ for different realizations of ξ. Note that other two probes are here considered to show additional phase portraits. The quality of agreement, as shown in this Figure, is the same among all probes considered in this study (not shown).

implies that large amplitude oscillations are affected by ν uncertainties in a stronger manner than the low amplitude counterparts.

From Figs. 6 and 7, it is also observed that igPC agrees very well with Monte-Carlo simulations. Although not shown in here, we highlight that an expansion of $P = 1$ is sufficient for accurately capturing the fields of $\mathbb{EE}$, $\mathbb{VE}$, $\mathbb{EV}$ and $\mathbb{VV}$ in case A.

Fig. 8 depicts a phase portrait of the two velocity components u and v. The control points correspond to probe ② and probe ⑤. The computation is done with an order of $P = 4$. Convergence results are achieved and no further improvement in the results is seen for $P > 4$. The gPC trajectories, both period-two and period-one limit cycles, agree very well with the deterministic counterpart, as also shown in Fig. 9.

We compare the stochastic signals of the horizontal velocity u in Fig. 10, which are extracted at probe ③ and ⑤. Whereas the signal measured at probe ③ exhibits two characteristic frequencies (a period-two limit cycle), the signal of probe ⑤ is related to only one characteristic frequency (a period-one limit cycle). The period-two limit cycle encloses the information of the vortex shedding from the upper and lower side of the bluff-body. Due to the modest computational cost we generated 4000 samples of gPC. By comparing the differences between estimators, it was considered sufficient to use 500 samples for the much more expensive MC simulations. It is observed that igPC not only captures the shape of the two type of signals, but also the crests. Only small differences are encountered in the spread of the realizations. This can be attributed to a very small frequency shift, that is captured by MC but not by igPC.

These signals are the basis for the PDFs shown in Fig. 11. The points in time chosen for evaluating the PDF are highlighted with blue lines in Fig. 10 and correspond to $[0, 0.125, 0.75]$ for probe ③ and $[0, 0.25, 0.5]$ for probe ⑤. The shape of the PDFs is fairly well recovered by igPC, where the mode is predicted approximately in the middle of the respective PDF. The support of the PDFs differs, which may arise from small frequency dependencies of the deterministic solution. To conclude: standard igPC can accurately predict the characteristic frequency and the amplitudes for all realizations, whereas the support of the PDFs is not perfectly reproduced.

6.3. Case B: uncertain inlet velocity

Consider the case of uncertain inlet velocity

$$u(\xi) = u_0 + u_1\xi, \quad \xi \in U[-1, 1], \tag{41}$$

with $u_0 = 100$ ms^{-1}, $u_1 = 5$ ms^{-1} while the viscosity $\nu = 1$ m^2 s^{-1} remains constant and deterministic. The range of Re investigated remains unchanged ($Re \in [95, 105]$) with respect to case A. For the simulations using igPC-ATI, we set $\alpha_0 = 8e{-}5$ and $\alpha_1 = 10$. A suitable set of parameters can be found by evaluating Δ (Eq. (15)) from previous simulations and adjusting α_0 and α_1 so that Eq. (19) has a fixed point for a large range of Δ.

We investigate the fields $\mathbb{EE}$, $\mathbb{VE}$, $\mathbb{EV}$ and $\mathbb{VV}$ in Figs. 12 and 13. It is observed that $\mathbb{EE}$ and $\mathbb{EV}$ remains unchanged with respect to case A. It means that the origin of uncertainties (either from ν or u inlet) do not play a role in the temporal mean value and vari-

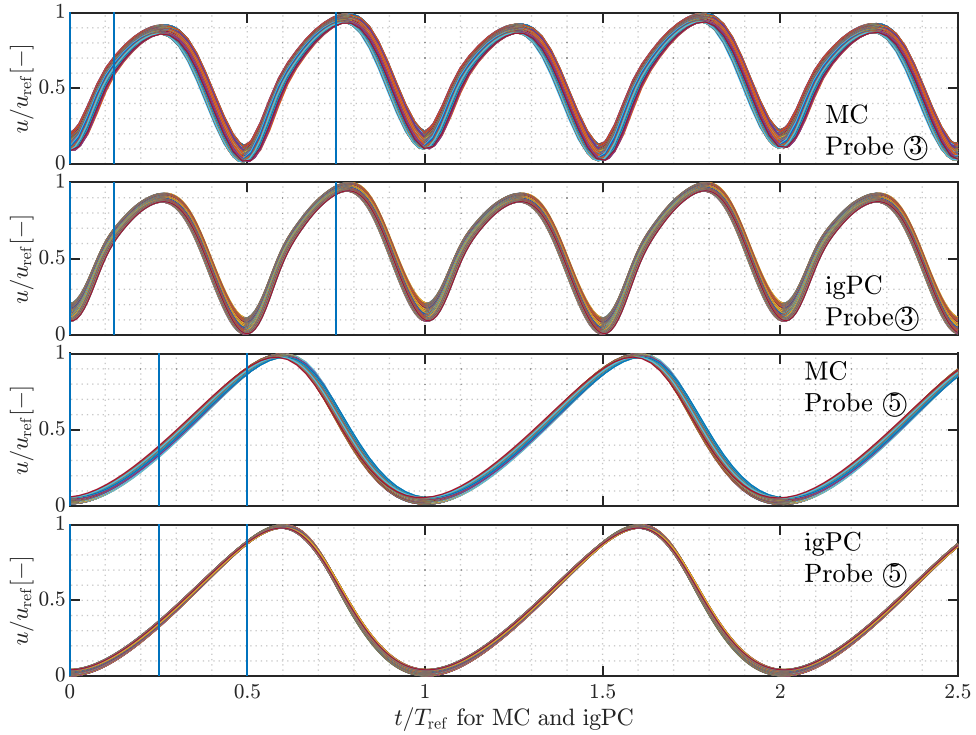

Fig. 10. Signals of the normalized u-velocity for probe ③ and ⑤ and different realizations of ξ compared to Monte Carlo. The results for igPC correspond to a simulation with $P = 4$.

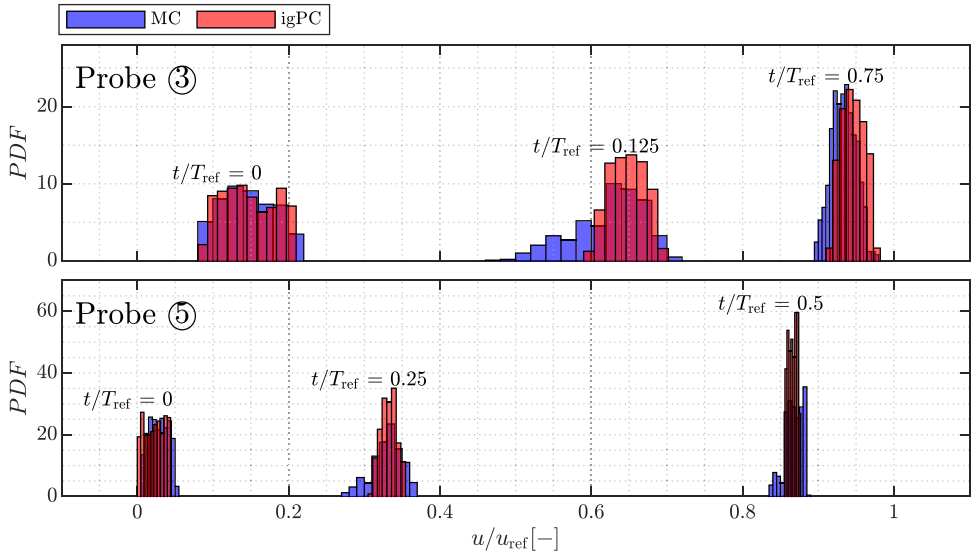

Fig. 11. PDFs of the normalized u-velocity for probe ③ and ⑤ and different snapshots of one period T_{ref} of the limit cycle for $P = 4$.

ance of the velocity oscillations. In contrast, the field of $\mathbb{VE}$ is very different with respect to the counterparts of case A, which implies that the propagation of uncertainties is, therefore, very different in case A and in case B. We observe in $\mathbb{VE}$ of case B that the dark blue region upstream of the bluff-body does not exist (as in case A), and it is now represented by a light blue-sky color. This is in agreement with the fact that the inlet velocity is constant but uncertain. We also observe that the regions of high velocity in $\mathbb{EE}$ (dark red) are also the regions more susceptible for uncertainties, as illustrated in $\mathbb{VE}$ (dark red). The field of $\mathbb{VV}$, contrary to $\mathbb{VE}$, is very similar in case A and in case B, yet the magnitudes are very different: the largest values of $\mathbb{VV}$ in case A are three times smaller than in case B. It means that the amplitude of the velocity limit cycles are more susceptible to uncertainties in the inlet velocity u than to uncertainties in ν.

Figs. 12 and 13 also show the fields $\mathbb{EE}$, $\mathbb{VE}$, $\mathbb{EV}$ and $\mathbb{VV}$ computed by igPC and igPC-ATI. Both techniques are able to accurately capture the fields $\mathbb{EE}$, $\mathbb{EV}$. We also observe that the uncertainty in $\mathbb{E}_t$ and $\mathbb{V}_t$, which is represented by $\mathbb{VE}$ and $\mathbb{VV}$, is not well captured by igPC. This is due to the fact that case B exhibits a stochastic frequency. Accordingly, the phase shift between realizations cannot be modelled by the standard igPC technique for low expansion orders (such as $P = 4$ chosen in this work). In contrast, igPC-ATI accurately captures the fields $\mathbb{VE}$ and $\mathbb{VV}$. Even an expansion with $P = 1$ is sufficient to reproduce all fields well (not shown). Since the higher modes of τ and $\boldsymbol{u}$ decay to a similar ex-

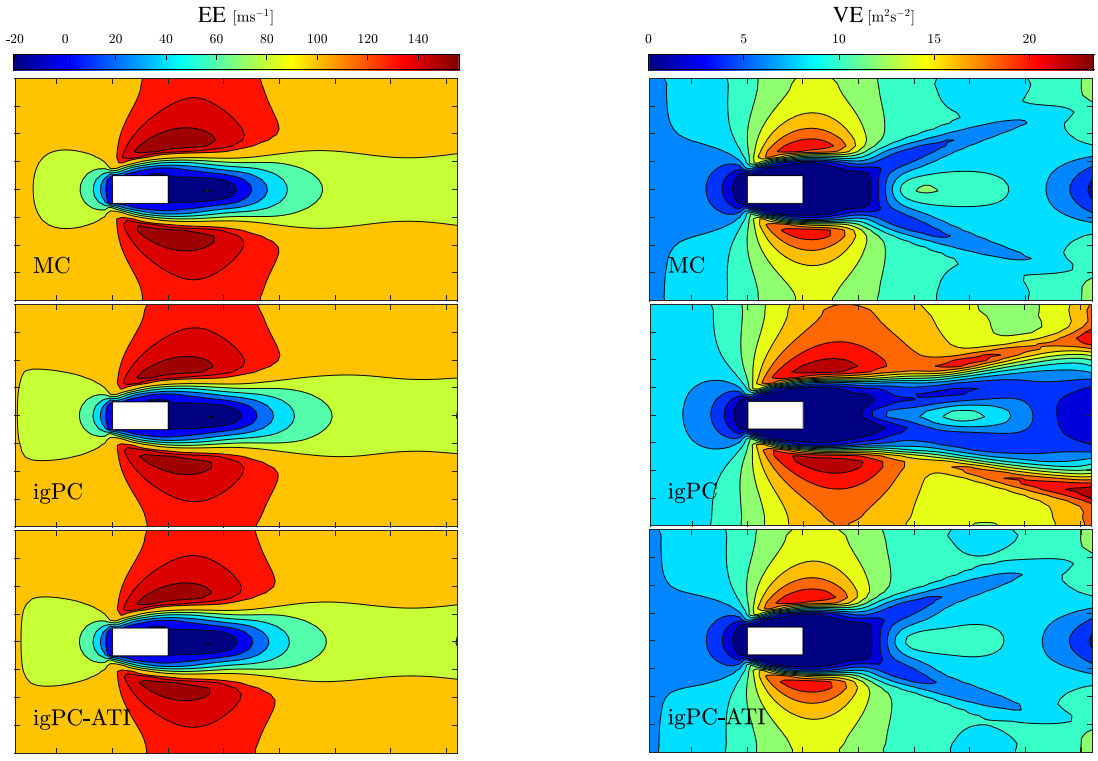

Fig. 12. Fields $\mathbb{EE}$ and $\mathbb{VE}$ for case B.

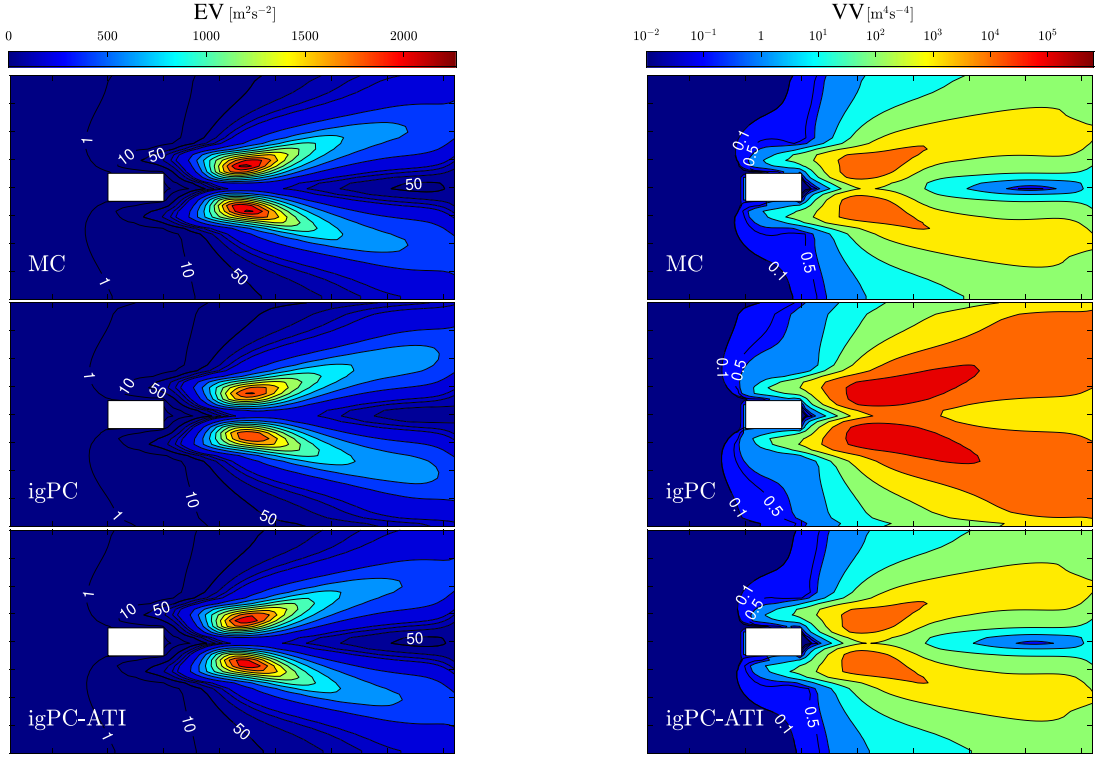

Fig. 13. Fields $\mathbb{EV}$ and $\mathbb{VV}$ for case B.

tent, it was considered sufficient to truncate the expansion of those quantities to the same polynomial order, which is also $P = 4$ for igPC-ATI.

We compare the phase portraits obtained by three deterministic simulations with the ones obtained by igPC and igPC-ATI. We consider the same locations as in case A. Fig. 14 shows a period-two limit cycle, whose amplitude slightly increases for increasing values of *Re*. This is in correspondence with case A, although in that case the trajectories are closer to each other (see Fig. 8). Fig. 14 also shows that igPC-standard fails when reproducing these trajectories, whereas igPC-ATI does a good job. The phase portraits illustrated in Fig. 15, taken at two different probes for different re-

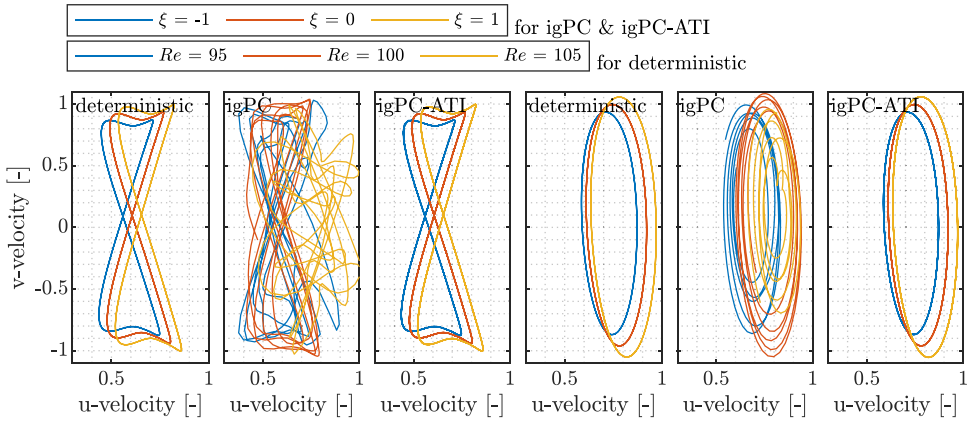

Fig. 14. Limit cycle oscillations for an uncertain inlet velocity for probe ② (left) and probe ⑤ (right) with $P = 4$ for different realizations of ξ.

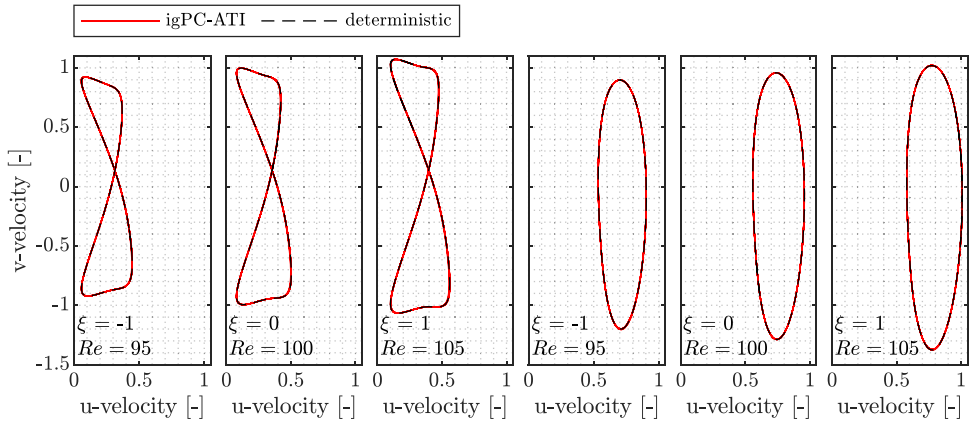

Fig. 15. Limit cycle oscillations for an uncertain inlet velocity for probe ① (left) and probe ⑥ (right) of the reference and the corresponding stochastic simulation with $P = 4$ for different realizations of ξ.

alizations of ξ, show a very good agreement with the reference simulation.

When looking at the signals of the horizontal velocity u that were measured for probe ③ and ⑤, the situation is similar to what was already indicated in the phase portraits. In Fig. 16, where all realizations or samples are shown, we can observe that standard igPC predicts spurious oscillations at probe ③ and cannot reproduce the correct amplitudes. In addition, another fact becomes clear at this point: standard igPC is not able to reconstruct a monotonic frequency shift between the realizations. The signal of standard igPC at probe ⑤ exhibits only a few predominant frequencies. These frequencies can be detected following the red lines, which correspond to $\xi \in [-1, -0.9]$ and $\xi \in [0.9, 1]$. Contrary to standard igPC, each realization created by igPC-ATI can be assigned its own time scale based on the information available from $\tau(\xi, t)$. The frequency shift predicted by Monte Carlo can therefore be reproduced well by asynchronous time integration.

Based on the signals of Fig. 16, PDFs are created for MC and igPC-ATI (Fig. 17). In contrast to case A, in which all realizations have the same frequency, the realizations are slightly shifted against each other for case B. Therefore, the PDFs at the corresponding snapshot have a larger support, what is adequately represented by igPC-ATI. In summary, igPC-ATI can reproduce the phase shift and predicts the amplitudes of the limit cycle very well, while standard igPC fails.

6.4. Computational costs

As part of the development of this work, simulations were also carried out with NigPC (standard and with time warping as proposed in Mai and Sudret [37]), by means of which the stochastic quantities could be reproduced at given times and spatial locations. The quality of the results is comparable to that of standard igPC and igPC-ATI. A computational cost comparison between NigPC (standard and with time warping) and igPC (standard and with ATI) is prone to sub-optimal implementations and other software constraints, such as memory allocation. We only comment on conceptual aspects that may reveal advantages and disadvantages of the respective methods.

The igPC method (standard or with ATI) may be well suited for the study of unsteady fields. In the cases investigated, we observe that the limit cycles are well resolved in time and space. Once the gPC coefficients – which are actually unsteady, spatial fields – are obtained, it is simple to carry out thorough uncertainty quantification, where the evolution of uncertainties can be accurately tracked in time and space. We observed that the igPC-ATI method is more expensive than the igPC counterpart, mainly due to the computational cost involved in solving the momentum equation. The latter is associated with a four-dimensional tensor $(\mathbb{E}_\xi(\Psi_i\Psi_j\Psi_k\Psi_m))$ in igPC-ATI and with a three-dimensional tensor $(\mathbb{E}_\xi(\Psi_i\Psi_j\Psi_k))$ in igPC.

If only the convective part $\sum_{i=0}^{P}\sum_{j=0}^{P}\mathbb{E}_{\boldsymbol{\xi}}\left(\Psi_i\Psi_j\Psi_k\right)(\boldsymbol{u}_i\cdot\nabla)\boldsymbol{u}_j$ of the expanded Navier–Stokes equations is considered as an example, we observe that the double sum above consists of as many terms as $\mathbb{E}_{\boldsymbol{\xi}}\left(\Psi_i\Psi_j\Psi_k\right)$ contains non-zero entries for a fixed k. If we assume that the total computational cost for evaluating the momentum equation is dominated by the number of terms in the summations, we conclude that the number of non-zero entries of the aforementioned tensors is an indicator of the computational time needed for solving the momentum equation.

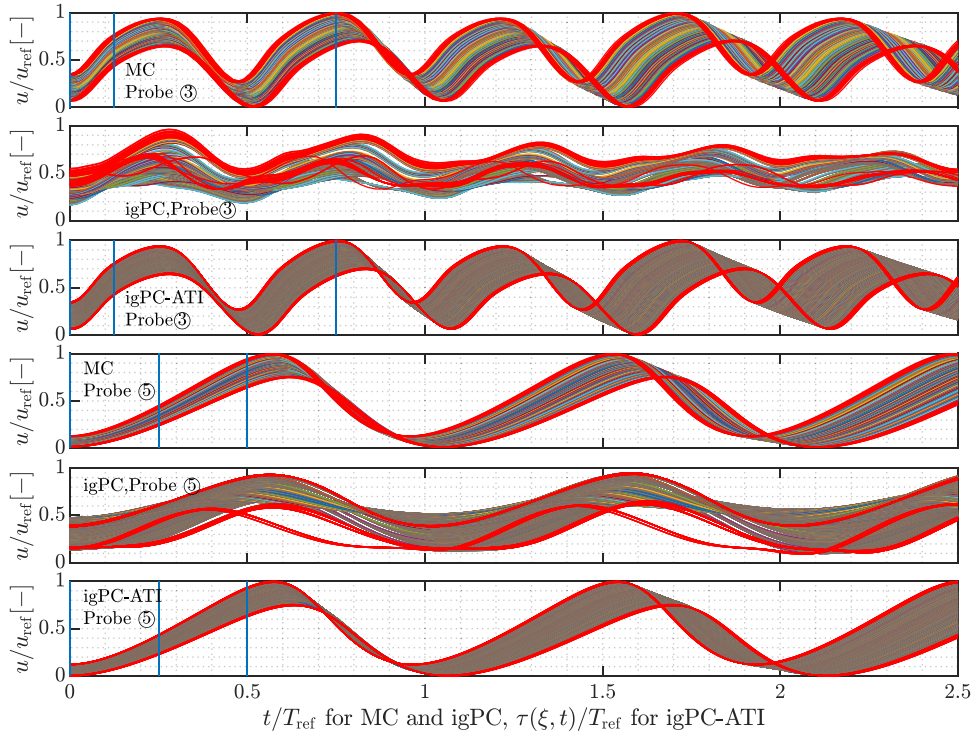

Fig. 16. Signals of the normalized u-velocity for probe ③ and ⑤ and different realizations of ξ compared to Monte Carlo. Realizations for $|\xi| > 0.9$ are marked in red. (For interpretation of the references to color in this figure legend, the reader is referred to the web version of this article.)

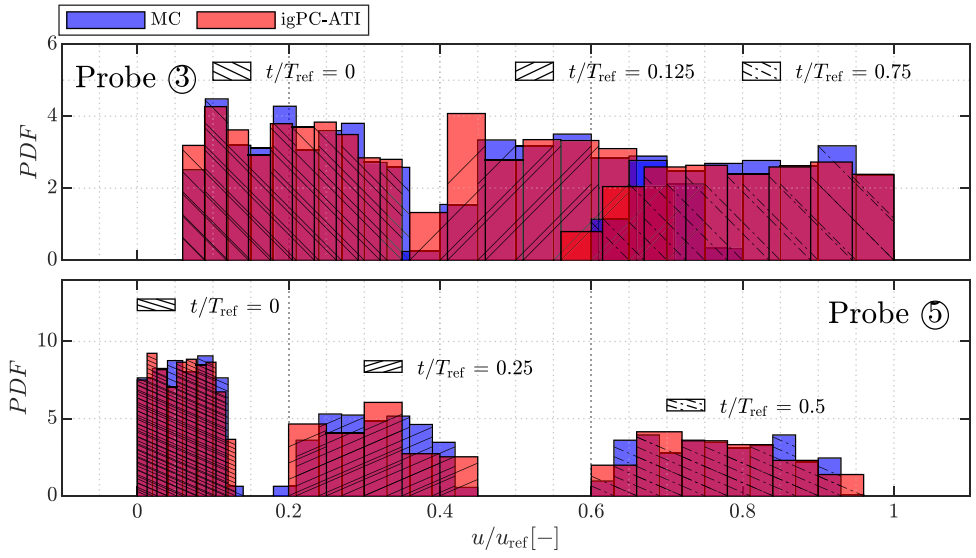

Fig. 17. PDFs of the normalized u-velocity for probe ③ and ⑤ and different snapshots of one period T_{ref} of the limit cycle related to $Re = 100$.

The computational cost related to the solution of the pressure-correction equation is comparable in both igPC and igPC-ATI, whereas the cost required for solving the ODE for the scalar vaue $\dot{\tau}$ (only needed in the igPC-ATI method) is negligible.

The computational cost associated with NigPC directly depends on the spatial and time resolution desired. For example, the computational cost derived from NigPC is clearly smaller than the one associated with igPC if only evaluations at a few spatial locations and instants of time within a period of the limit cycle are needed. In contrast, if highly resolved fields in time and space are required, the methods igPC and igPC-ATI may become competitive with respect to NigPC (standard or time warping) in terms of computational efficiency. The tests we made depend on one random variable only, but if we extrapolate clock-times to multi-variate problems, it seems that igPC might be more performing than NigPC for small polynomial order p and moderate number of uncertain input variables n. More work should be done on this matter before drawing final conclusions.

7. Discussion and conclusions

Intrusive generalized polynomial chaos has been applied to the Kármán vortex street. The difference compared to the standard igPC approach is the implementation of a local time for each realization via asynchronous time integration, which enables to properly capture limit cycles with stochastic frequency. Using different

flow setups that increase in complexity, we demonstrate the capabilities and limits of igPC in its standard form and with ATI:

- Standard igPC is suitable for the computation of time-dependent, space-dependent PDFs of periodic flow fields with deterministic oscillation frequency. One such problem is the Kármán vortex street, subject to a stochastic viscosity. A small number of terms in the expansion ($P+1=5$) is sufficient to ensure a good representation of the individual trajectories in the phase portraits. Results based on $P=1$ for (steady) statistic fields $\mathbb{EE}$, $\mathbb{EV}$, $\mathbb{VE}$ and $\mathbb{VV}$ are already a good estimate. Relevant applications for standard igPC could be confined flows in the laminar regime, where uncertainties in the temperature affect the viscosity of the fluid.
- Standard igPC cannot provide reliable results for problems with stochastic frequencies. Only the quantities $\mathbb{EE}$ and $\mathbb{EV}$ are correctly reproduced. Limit cycles are not well recovered. We observe large deviations for the trajectories and unusual dynamics, as already described in previous works.
- We demonstrate that the ATI-method, which was originally introduced for linear ODEs, can be successfully applied to the incompressible Navier–Stokes equations. This technique offers a remedy to problems with stochastic QoIs under the assumption that the frequency is a smooth function of the random inputs. We demonstrate that the trajectories of the limit cycles are in very good agreement with the deterministic reference. The statistic fields and the PDFs match the results of Monte Carlo simulations.

Further extensions of this numerical method could combine the benefits from non-intrusive and intrusive approaches. Since an unstable fixed point $\dot{\tau}^*$ can make it difficult to solve the ODE for $\dot{\tau}$, it is desirable that the stochastic clock $\tau(\boldsymbol{\xi},t)$ is known in advance. Such a relation could be determined beforehand by NigPC and time warping (with small values of polynomial order p). Additionally, if we know where in the parameter space the frequency is non-smooth, we could introduce igPC-ATI separately on the piecewise smooth regions.

The present work contributes to the understanding of the gPC method for the solution of unsteady, periodic laminar flow problems.

Declaration of Competing Interest

The authors declare that they have no known competing financial interests or personal relationships that could have appeared to influence the work reported in this paper.

Appendix A. Discretization of the stochastic incompressible Navier–Stokes equations

In this appendix we propose a method to solve the discretized versions of Eqs. (27) and (28) to compute the modes in (8).

To avoid the well-known checkerboard problem, we use Rhie and Chow interpolation on collocated grids, where pressure and velocity are decoupled [53]. Additionally, we implement a predictor-corrector scheme, better known as fractional-step method, which was developed by [54] and improved by Goda [55]. As this algorithm allows to solve the pressure equation only once per time step, it is widely used in unsteady flow simulations. First, the intermediate stochastic velocity modes $\boldsymbol{u}_k^*$ are calculated by adding the pressure gradient evaluated at time step n. This can be denoted as the predictor step:

$$\frac{\boldsymbol{u}_k^*-\boldsymbol{u}_k^n}{\Delta t}=\boldsymbol{H}_k^n-\frac{1}{\rho}\nabla p_k^n, \tag{A.1}$$

where Δt is the time step and the term $\boldsymbol{H}_k^n$ represents the gPC expanded convective and diffusive terms derived in Eq. (28):

$$\boldsymbol{H}_k^n=-\sum_{i=0}^{P}\sum_{j=0}^{P}\mathbb{E}_{\boldsymbol{\xi}}\big(\Psi_i\Psi_j\Psi_k\big)(\boldsymbol{u}_i^n\cdot\nabla)\boldsymbol{u}_j^n+\sum_{i=0}^{P}\sum_{j=0}^{P}\mathbb{E}_{\boldsymbol{\xi}}\big(\Psi_i\Psi_j\Psi_k\big)\nu_i\nabla^2\boldsymbol{u}_j^n. \tag{A.2}$$

System (A.1) is solved coupled, which means that a new solver must be written for the expanded system and the deterministic solver cannot be used here. The final velocity at the new time level requires the gradient of the pressure at time step $n+1$. The equation for the corrector step reads

$$\frac{\boldsymbol{u}_k^{n+1}-\boldsymbol{u}_k^n}{\Delta t}=\boldsymbol{H}_k^n-\frac{1}{\rho}\nabla p_k^{n+1}. \tag{A.3}$$

By means of subtracting Eq. (A.1) from (A.3), an expression for velocity correction $\boldsymbol{u}_k^{n+1}-\boldsymbol{u}_k^*$ results in

$$\frac{\boldsymbol{u}_k^{n+1}-\boldsymbol{u}_k^*}{\Delta t}=-\frac{1}{\rho}\nabla\hat{p}_k, \tag{A.4}$$

in which $\hat{p}_k$ is an abbreviation for the pressure correction $p_k^{n+1}-p_k^n$. By applying divergence to Eq. (A.4) and making use of the continuity constraint $\nabla\cdot\boldsymbol{u}_k^{n+1}=0$, one can write the Poisson equation for the pressure correction $\hat{p}_k$ as

$$\nabla^2\hat{p}_k=\frac{\rho}{\Delta t}\nabla\cdot\boldsymbol{u}_k^*. \tag{A.5}$$

The pressure correction can be solved individually for every mode k of pressure $\hat{p}$ because the modes are decoupled. As a last step, Eq. (A.4) is used to obtain the velocity field at the new time step $n+1$ and the pressure is corrected by $p_k^{n+1}=p_k^n+\hat{p}_k$.

Appendix B. Stochastic expansion of the clock speed $\dot{\tau}$

The deterministic equation for the clock speed already mentioned in Eq. (19) reads

$$\frac{d}{dt}\dot{\tau}(\boldsymbol{\xi},t)=-\alpha_0\dot{\tau}(\boldsymbol{\xi},t)\Delta(\boldsymbol{\xi},t))+\alpha_1(1-\dot{\tau}(\boldsymbol{\xi},t)), \tag{B.1}$$

where $\Delta(\boldsymbol{\xi},t)$ is defined at a specific location as

$$\Delta=\big(\boldsymbol{u}(\boldsymbol{\xi},t)-\boldsymbol{u}^{(r)}(t)\big)\cdot\mathcal{F}^{(r)}(\boldsymbol{u}^{(r)}(t)). \tag{B.2}$$

The reference solution associated with $\mathcal{F}^{(r)}(\boldsymbol{u}^{(r)}(t))$ is the case $Re=100$, which corresponds to the realization $\xi=0$. In detail, only the phase of a single point in the domain of this reference model is used. In our work, this point belongs to Probe ②. Inserting the formulation in Eq. (B.2) for Δ into Eq. (B.1), we arrive at the expression

$$\frac{d}{dt}\dot{\tau}(\boldsymbol{\xi},t)=-\alpha_0\dot{\tau}(\boldsymbol{\xi},t)\Big[\big(\boldsymbol{u}(\boldsymbol{\xi},t))-\boldsymbol{u}^{(r)}(t)\big)\cdot\mathcal{F}^{(r)}\Big]+\alpha_1\big(1-\dot{\tau}(\boldsymbol{\xi},t)\big), \tag{B.3}$$

where we have neglected the argument of $\mathcal{F}^{(r)}(\boldsymbol{u}^{(r)}(t))$ for reasons of readability. After applying the gPC expansion and the stochastic projection on the polynomial basis, the equation reads

$$\begin{aligned}\frac{d\dot{\tau}_k}{dt}=&-\alpha_0\sum_{i=0}^{P}\sum_{j=0}^{P}\mathbb{E}_{\boldsymbol{\xi}}\big(\Psi_i\Psi_j\Psi_k\big)\dot{\tau}_i\Big[\big(\boldsymbol{u}_j-\boldsymbol{u}^{(r)}(t)\big)\cdot\mathcal{F}^{(r)}\Big]\\&+\mathbb{E}_{\boldsymbol{\xi}}(\Psi_k)\alpha_1-\alpha_1\dot{\tau}_k,\end{aligned} \tag{B.4}$$

in which the dependency on $\boldsymbol{\xi}$ and t of some variables is again not shown because of readability purposes. Note that P is chosen identical for the velocity $\boldsymbol{u}$ and the clock time $\dot{\tau}$, since these quantities show a similar convergence behavior with respect to P.

This ODE is solved using the implicit Euler method and its behavior is strongly dependent on the parameters α_0 and α_1. The numerical values selected in this work for igPC-ATI ($P=4$) are $\alpha_0=8e-5$ and $\alpha_1=10$.

Supplementary material

Supplementary material associated with this article can be found, in the online version, at 10.1016/j.compfluid.2021.104952

CRediT authorship contribution statement

P. Bonnaire: Conceptualization, Writing - original draft, Writing - review & editing. **P. Pettersson:** Conceptualization, Writing - original draft, Writing - review & editing. **C.F. Silva:** Conceptualization, Writing - original draft, Writing - review & editing.

References

[1] Ghanem RG, Spanos PD. Stochastic finite elements: a spectral approach. Courier Corporation; 1991.
[2] Xiu D, Karniadakis GE. The Wiener–Askey polynomial chaos for stochastic differential equations. SIAM J Sci Comput 2002;24(2):619–44.
[3] Le Maître OP, Knio OM. Spectral methods for uncertainty quantification: with applications to computational fluid dynamics. Springer Science & Business Media; 2010.
[4] Najm HN. Uncertainty quantification and polynomial chaos techniques in computational fluid dynamics. Annu Rev Fluid Mech 2009;41:35–52.
[5] Lucor D, Meyers J, Sagaut P. Sensitivity analysis of large-eddy simulations to subgrid-scale-model parametric uncertainty using polynomial chaos. J Fluid Mech 2007;585:255–79.
[6] Congedo PM, Duprat C, Balarac G, Corre C. Numerical prediction of turbulent flows using Reynolds-averaged Navier–Stokes and large-eddy simulation with uncertain inflow conditions. Int J Numer Methods Fluids 2013;72(3):341–58.
[7] Hosder S, Maddalena L. Non-intrusive polynomial chaos for the stochastic CFD study of a supersonic pressure probe. AIAA Pap 2009;1129.
[8] Reagan MT, Najm HN, Ghanem RG, Knio OM. Uncertainty quantification in reacting-flow simulations through non-intrusive spectral projection. Combust Flame 2003;132(3):545–55.
[9] Khalil M, Lacaze G, Oefelein JC, Najm HN. Uncertainty quantification in LES of a turbulent bluff-body stabilized flame. Proc Combust Inst 2015;35(2):1147–56.
[10] Migliorati G, Nobile F, von Schwerin E, Tempone R. Approximation of quantities of interest in stochastic PDEs by the random discrete L^2 projection on polynomial spaces. SIAM J Sci Comput 2013;35:A1440–60.
[11] Blatman G, Sudret B. Adaptive sparse polynomial chaos expansion based on least angle regression. J Comput Phys 2011;230(6):2345–67.
[12] Hampton J, Doostan A. Compressive sampling of polynomial chaos expansions: convergence analysis and sampling strategies. J Comput Phys 2015;280:363–86.
[13] Todor RA, Schwab C. Convergence rates for sparse chaos approximations of elliptic problems with stochastic coefficients. IMA J Numer Anal 2007;27(2):232–61.
[14] Bachmayr M, Cohen A, Migliorati G. Sparse polynomial approximation of parametric elliptic PDEs. Part I: affine coefficients. ESAIM 2017;51(1):321–39.
[15] Bachmayr M, Cohen A, DeVore R, Migliorati G. Sparse polynomial approximation of parametric elliptic PDEs. Part II: lognormal coefficients. ESAIM 2017;51(1):341–63.
[16] Cohen A, DeVore R, Schwab C. Analytic regularity and polynomial approximation of parametric and stochastic elliptic PDEs. Anal Appl 2011;9(01):11–47.
[17] Bäck J, Nobile F, Tamellini L, Tempone R. Stochastic spectral Galerkin and collocation methods for PDEs with random coefficients: a numerical comparison. In: Hesthaven JS, Rønquist EM, editors. Spectral and high order methods for partial differential equations. Berlin, Heidelberg: Springer Berlin Heidelberg; 2011. p. 43–62. ISBN 978-3-642-15337-2.
[18] Beck J, Tempone R, Nobile F, Tamellini L. On the optimal polynomial approximation of stochastic PDEs by Galerkin and collocation methods. Math Models Methods Appl Sci 2012;22(09):1250023.
[19] Blatman G, Sudret B. Sparse polynomial chaos expansions and adaptive stochastic finite elements using a regression approach. CR Méc 2008;336(6):518–23.
[20] Alekseev AK, Navon IM, Zelentsov ME. The estimation of functional uncertainty using polynomial chaos and adjoint equations. Int J Numer Methods Fluids 2011;67(3):328–41.
[21] Onorato G, Loeven GJA, Ghorbaniasl G, Bijl H, Lacor C. Comparison of intrusive and non-intrusive polynomial chaos methods for CFD applications in aeronautics. In: V European conference on computational fluid dynamics ECCOMAS, Lisbon, Portugal; 2010. p. 14–17.
[22] Le Maître OP, Knio OM, Najm HN, Ghanem RG. A stochastic projection method for fluid flow. J Comput Phys 2001;173(2):481–511.
[23] Le Maître OP, Reagan MT, Najm HN, Ghanem RG, Knio OM. A stochastic projection method for fluid flow: II. Random process. J Comput Phys 2002;181(1):9–44.
[24] Lucor D, Karniadakis GE. Noisy inflows cause a shedding-mode switching in flow past an oscillating cylinder. Phys Rev Lett 2004;92(15):154501.
[25] Mathelin L, Hussaini MY, Zang TA. Stochastic approaches to uncertainty quantification in CFD simulations. Numer Algorithms 2005;38(1–3):209–36.
[26] Herzog M, Gilg A, Paffrath M, Rentrop P, Wever U. Intrusive versus non-intrusive methods for stochastic finite elements. In: From nano to space. Springer; 2008. p. 161–74.
[27] Pettersson P, Iaccarino G, Nordström J. Numerical analysis of the Burgers' equation in the presence of uncertainty. J Comput Phys 2009;228(22):8394–412.
[28] Knio O, Le Maître O. Uncertainty propagation in CFD using polynomial chaos decomposition. Fluid Dyn Res 2006;38(9):616–40.
[29] Pettersson P, Nordström J, Doostan A. A well-posed and stable stochastic Galerkin formulation of the incompressible Navier–Stokes equations with random data. J Comput Phys 2016;306:92–116.
[30] Wiener N. The homogeneous chaos. Am J Math 1938;60(4):897–936.
[31] Orszag SA, Bissonnette LR. Dynamical properties of truncated Wiener–Hermite expansions. Phys Fluids 1967;10(12):2603–13.
[32] Hou TY, Luo W, Rozovskii B, Zhou H-M. Wiener chaos expansions and numerical solutions of randomly forced equations of fluid mechanics. J Comput Phys 2006;216(2):687–706.
[33] Wan X, Karniadakis GE. Long-term behavior of polynomial chaos in stochastic flow simulations. Comput Methods Appl MechEng 2006;195(41–43):5582–96.
[34] Gerritsma M, van der Steen J-B, Vos P, Karniadakis G. Time-dependent generalized polynomial chaos. J Comput Phys 2010;229(22):8333–63.
[35] Le Maître OP, Mathelin L, Knio OM, Hussaini M. Asynchronous time integration for polynomial chaos expansion of uncertain periodic dynamics. Discrete Contin Dyn Syst 2010;28(1):199–226.
[36] Schick M, Heuveline V, Le Maître OP. A Newton–Galerkin method for fluid flow exhibiting uncertain periodic dynamics. SIAM/ASA J Uncertain Quantif 2014;2(1):153–73.
[37] Mai CV, Sudret B. Surrogate models for oscillatory systems using sparse polynomial chaos expansions and stochastic time warping. SIAM/ASA J Uncertain Quantif 2017;5(1):540–71.
[38] Giraldi L, Le Maître OP, Mandli K, Dawson C, Hoteit I, Knio OM. Bayesian inference of earthquake parameters from buoy data using a polynomial chaos-based surrogate. Comput Geosci 2017:683–99.
[39] Colombo I, Nobile F, Porta G, Scotti A, Tamellini L. Uncertainty quantification of geochemical and mechanical compaction in layered sedimentary basins. Comput Methods Appl MechEng 2018;328:122–46.
[40] Sapsis TP, Lermusiaux PF. Dynamically orthogonal field equations for continuous stochastic dynamical systems. Phys D 2009;238(23):2347–60.
[41] Musharbash E, Nobile F, Zhou T. Error analysis of the dynamically orthogonal approximation of time dependent random PDEs. SIAM J Sci Comput 2015;37(2):A776–810.
[42] Sapsis TP, Lermusiaux PF. Dynamical criteria for the evolution of the stochastic dimensionality in flows with uncertainty. Phys D 2012;241(1):60–76.
[43] Musharbash E, Nobile F. Dual dynamically orthogonal approximation of incompressible Navier–Stokes equations with random boundary conditions. J Comput Phys 2018;354:135–62.
[44] Shen J, Wang L-L. Sparse spectral approximations of high-dimensional problems based on hyperbolic cross. SIAM J Numer Anal 2010;48(3):1087–109.
[45] Ernst OG, Ullmann E. Stochastic Galerkin matrices. SIAM J Matrix Anal Appl 2010;31(4):1848–72.
[46] Mallock HRA. On the resistance of air. Proc R Soc Lond A 1907;79(530):262–73.
[47] Bénard H. Formation périodique de centres de giration á l'arriére d'un obstacle en mouvement. CR Acad Sci Paris 1908;147:839–42.
[48] Kármán Tv. Ueber den mechanismus des widerstandes, den ein bewegter körper in einer flüssigkeit erfährt. Nachr Ges Wiss Gött Math-Phys Klasse 1911;1911:509–17.
[49] Okajima A. Strouhal numbers of rectangular cylinders. J Fluid Mech 1982;123(-1):379–98.
[50] Okajima A, Nagahisa T, Rokugou A. A numerical analysis of flow around rectangular cylinders. Jpn Soc Mech Eng Ser B 1990;56(522):280–8.
[51] Sohankar A, Norberg C, Davidson L. Numerical simulation of unsteady low-Reynolds number flow around rectangular cylinders at incidence. J Wind Eng Ind Aerod 1997;69–71:189–201.
[52] Islam SU, Zhou CY, Shah A, Xie P. Numerical simulation of flow past rectangular cylinders with different aspect ratios using the incompressible lattice Boltzmann method. J Mech Sci Technol 2012;26(4):1027–41.
[53] Rhie CM, Chow WL. Numerical study of the turbulent flow past an airfoil with trailing edge separation. AIAA J 1983;21(11):1525–32.
[54] Chorin AJ. Numerical solution of the Navier–Stokes equations. Math Comput 1968;22(104):745–62.
[55] Goda K. A multistep technique with implicit difference schemes for calculating two- or three-dimensional cavity flows. J Comput Phys 1979;30(1):76–95.